scientific reports

OPEN

Structural, magnetic, and optical characteristics of undoped and chromium, iron, cobalt, copper, and zinc doped nickel oxide nanopowders

Farzaneh Asaldoust[1], **Khosro Mabhouti**[1]✉, **Akbar Jafari**[1] & **Maryam Taleb-Abbasi**[2]

The present investigation seeks to customize the optical, magnetic, and structural characteristics of nickel oxide (NiO) nanopowders through chromium, iron, cobalt, copper, and zinc doping to enhance optoelectronic applications. In this regard, the preparation of pristine NiO and $Ni_{0.95}X_{0.05}O$ (X = Cr, Fe, Co, Cu, and Zn) powders was successfully achieved through the co-precipitation method. The X-ray powder diffraction was employed to examine the prepared powders' phase formation and crystal structure characteristics. The obtained results revealed the presence of a face-centered cubic structure in all samples. In addition, doping of Cr, Fe, Co, Cu, and Zn into the NiO system did not induce any other secondary phase. Moreover, the estimation of the crystalline size for the pristine and doped samples was carried out using the Debye-Scherrer formula, yielding values ranging from 16 to 28 nm which is deemed suitable for the study of doping effects. Moreover, the morphological characteristics of both the pristine and doped NiO powders were investigated using a field emission scanning electron microscope coupled with energy dispersive spectroscopy to confirm the presence of dopant elements and chemical composition. The morphological results revealed the growth of homogeneous nanocrystallites with fine particles. Furthermore, the samples underwent Fourier Transform Infrared Spectroscopy analysis to validate their purity, which revealed the presence of vibrational modes in the metal oxide bonds. An optical investigation was conducted on all samples utilizing a diffuse reflectance spectroscopy within the spectral range of 350–900 nm. Band gap values were estimated based on diffuse reflectance spectroscopy data through Tauc plot analysis, yielding a range from 2.77 to 3.46 eV. This analysis revealed a red shift in NiO with all dopants except for Zn doping. Additionally, numerical calculations utilizing the Kramers–Kronig relation were performed to assess the extinction coefficient (k) and refractive index (n) parameters from the reflectance data. The presence of room-temperature ferromagnetism was elucidated in all samples by the findings acquired through the application of the vibrating sample magnetometer technique. The parameters of coercivity exhibit an increase from 80.44 Oe for pristine NiO to 350.75 Oe for Zn-doped NiO, a phenomenon that is advantageous for applications in data storage. The introduction of iron into NiO nanoparticles has profoundly affected the magnetic properties, resulting in a transition of the material from a weak ferromagnetic state to a ferromagnetic state. The outcomes imply promising magnetic and optical applications for such earlier mentioned nanopowders. This observation suggests that the prepared NiO nanopowders have significant potential in both linear and nonlinear optical devices, optoelectronics, and data storage technologies.

Keywords Nickle oxide nanoparticles, Structural properties, Optical properties, Magnetic properties, Kramers–Kronig

The preparation of transition metal (TM) oxide possesses distinct morphological characteristics, well-defined composition, finite dimensions, and crystallite size smaller than approximately 100 nm, assume a significant role

[1]Department of Physics, Faculty of Sciences, Urmia University, Urmia, Iran. [2]Department of Physical Chemistry, Faculty of Chemistry, University of Tabriz, Tabriz, Iran. ✉email: kh.mabhouti@urmia.ac.ir

in the storage process and the conversion of the energy of the materials, thereby contributing to the sustained progress of humanity[1]. Furthermore, TM oxides have garnered much attention among researchers due to their noteworthy optical, catalytic, thermal, magnetic, and electronic properties compared to larger-scale equivalents. Also, they are extensively examined in both their nano and macro scales due to their applicability and feasibility[2]. Among the TM oxides, Nickel oxide (NiO) is subject to significant experimental and theoretical research due to its focus on the advancement of p-type semiconductors and the study of highly correlated electron systems[3]. NiO is widely acknowledged as an insulator of the charge-transfer type, an insulator of the Mott Hubbard type, characterized by a wide energy gap of approximately 3 to 4 electron volts and a conductivity of approximately 10^{-13} Siemens per centimeter, distinguished by its high boiling and melting points, and is renowned for its considerable stability in both thermal and chemical environments[4]. The structure of NiO is cubic with a face-centered cubic (FCC) arrangement and belongs to the space group fm3m. Furthermore, NiO stands out due to several key features. First, it is characterized by low toxicity and can be synthesized cost-effectively. Second, NiO exhibits intriguing electrochromic behavior, making it suitable for applications in bright windows and displays. Third, the material demonstrates multiple valence states of nickel, including Ni^{2+} and Ni^{3+}, contributing to its versatile behavior. Lastly, NiO possesses a high surface-to-volume ratio, enhancing its reactivity and potential use in catalysis and sensing applications[5]. Especially, in its bulk state, NiO demonstrates an antiferromagnetic behavior, which is of a great interest for fundamental studies and potential spintronic applications[6]. However, when NiO is in nanostructured form, it exhibits ferromagnetic properties even at ambient temperature[7]. The electrochromic, electrical, exceptional optical, magnetic, and structural characteristics of NiO render them exceptionally appropriate for a diverse array of applications, encompassing, but not confined to, drug delivery, battery cathodes, UV photodetectors, magnetic memory devices, nano-electronic devices, photo-catalysts, sensors, solar cells, supercapacitors, intelligent windows, thin film transistors, magnetic bar codes, and spintronic devices[8]. The optical characteristics of NiO have been examined by Newman, Powell, and Low[9–11], however, Kleemann and Rodionov have studied the optical absorbance spectra of NiO[12,13]. These investigations propose that NiO, a p-type semiconductor, has the potential to be employed in diverse applications like super-paramagnetic, antimicrobial agents, heterogeneous catalytic materials, and electronic and optical devices. These devices include p-type transparent conductor films, sensors, solid oxide fuel cells, dye-sensitized solar cells, alkaline battery cathodes and electrochromic films[14].

However, the attributes of NiO are constrained when employed in its bulk stoichiometric state and necessitate further advancements to augment its usability. Changing the stoichiometry of NiO can be achieved by intrinsically incorporating dopants during the preparation under external or regulated circumstances exhibiting novel constituents, such as alkaline earth metal and TM elements[15]. Chemical doping has been employed in synthesizing to acquire enhanced magnetic, structural, and optical characteristics of NiO nanoparticles for diverse applications[2]. The magnetic properties of NiO can be adjusted by substituting Ni with TM ions. Balaraju Bayappagari et al.[16] reported the optical, magnetic, and structural characteristics of NiO nanopowders doped with iron and manganese. They found that both synthesized samples exhibited a distinct hysteresis loop and a noticeable augmentation in saturation magnetic moment as the annealing temperature increased. Rinaldi-Montes et al.[17] have reported that NiO, conventionally known for its antiferromagnetic properties in its bulk state, demonstrates ferromagnetic characteristics at the nano-size due to nickel vacancy defects. It has been observed that the magnetic moment of NiO steadily amplifies as the particle size decreases. Li et al.[18] investigated the impact of doping of the copper on the nickel oxide thin films for their resistive switching. The study revealed that copper replaces nickel with a valence of + 1 and enhances the presence of oxygen vacancies, which govern the process of switching. Using the co-precipitation technique, Yousaf et al.[19] synthesized pristine NiO nanoparticles and Zn and Cu-doped NiO nanopowders. The resulting nanoparticles were found to be in the size range of 10–20 nm and single phase. The doped nanoparticles were found to have a reduced band gap, which enhanced their photocatalytic activity. Furthermore, the substitution of Cu^{2+} ions in the nanoparticles led to an increase in conductivity. Just recently, P. Soumya Menon et al.[20] have reported the significance of surface imperfections in the optical characteristics of pure NiO and chromium-doped NiO nanostructures. Cu is a TM element with multiple valences, specifically + 1 and + 2. It is possible to incorporate Cu ions into the crystal lattice of NiO without causing any damage to its crystal structure or microstructural properties. This phenomenon has been observed in previous studies[21]. Cu impurities and oxygen vacancy formation energies near Cu sites are relatively low. Additionally, it has been noted that copper atoms do not exhibit a propensity for cluster formation, and materials containing Cu are non-ferromagnetic. This characteristic of Cu-based compounds successfully addresses the issue of magnetic precipitate formation, thereby overcoming the associated challenge[22]. In addition, Cu exhibits comparable ionic radii with Ni, as indicated by the Shannon ionic radii in octahedral arrangement (Cu^{+}: 0.77 Å, Cu^{2+}: 0.73 Å, Ni^{2+}: 0.69 Å, and Ni^{3+}: 0.60 Å)[23]. Furthermore, Cu and Ni possess closely aligned electronegativity values of 1.9 and 1.91, respectively, by the Pauling scale[24]. Zinc is a prospective TM constituent that can be employed as a fitting supplement for nickel oxide owing to its closely aligned ionic radius parameter. Furthermore, the comprehensive understanding of the diverse physical attributes of Zn-doped NiO nanostructures remains restricted[25]. Because of the different 3d electron configurations of Zn^{2+} ($3d^{10}$) and Ni^{2+} ($3d^{8}$), substituting Ni^{2+} with Zn^{2+} is expected to affect NiO's magnetic and optical properties[26]. The introduction of Cobalt doping can augment the conductivity of Nickel Oxide, a factor that proves advantage in enhancing electrochromic and energy density performance[27]. Chromium (Cr) is utilized across diverse domains, including catalysts, paints, inks, refractory substances, corrosion-resistant substances, and optoelectronic devices. Research on the doping of NiO with chromium is very rare[28]. Adding Cr as a dopant results in a stable phase and an enhancement in electrical conductivity in NiO. Moreover, Cr exhibits a range of oxidation states, and its ionic radius is nearly equivalent to that of Ni, rendering it a suitable dopant for NiO[29]. The structural and magnetic characteristics undergo notable changes upon Fe doping. The magnetic behavior of NiO could be reinforced by doping with TM ions, such as Fe^{3+}, leading to a shift towards an improved ferromagnetic state[30]. In a study conducted by Jianfei Wang et al.[31], it was observed that Fe-doped NiO nanoparticles exhibit ferromagnetism even at ambient temperature. Manna et al.[32] reported that reducing the size of TM ions in NiO nanoparticles is crucial for the emergence of the ferromagnetic phase, primarily due to an uncompensated spin sublattice. Mishra et al.[33] discovered that a concentration of the dopant level below 3% results in a minimal phase, and magnetic changes cannot be ascertained using XRD. The synthesis of NiO nanoparticles has been carried out through several methods, such as the thermal decomposition method[34], the sonochemical method[35], the solvothermal method[36], the hydrothermal method[37], the sol-gel process[38], and the co-precipitation approach[39]. Among the various techniques available, co-precipitation emerges as a prominent method for the preparation of nanoparticles. This approach entails the reduction of the reaction temperature, thereby facilitating the uniform precipitation of the reagents. It serves as a straightforward means of synthesizing nanopowders made of metal oxides, which exhibit elevated reactivity levels during sintering at low temperatures. In addition, the coprecipitation technique is recognized for its cost-effectiveness, energy efficiency, and simplicity. Based on our knowledge, there is no comprehensive literature on the simultaneous synthesis and investigation of the properties of all the mentioned dopants with a doping percentage of 5%. Therefore, in this research, NiO and $Ni_{0.95}\times_{0.05}O$ powders (X = Cr, Fe, Co, Cu, and Zn) were successfully obtained through the co-precipitation method and by optimizing the appropriate calcination temperature separately for each doping element. Given that the main parameters of nanoparticles, including the size, shape, and structure of individual particles, as well as their spatial distribution, affect the properties of the nanoparticle system and lead to special optical properties that can be used, in new material applications[40]. Therefore, the calcination temperature was optimized to convert hydroxide to metal oxide and strengthen the properties of nanoparticles by producing larger nanoparticles. In addition, the Kramers-Kronig (K-K) numerical relations[41] can be used, to evaluate the linear properties of nanoparticles. The K-K dispersion relation has been used to obtain the optical parameters of NPs with the support of DRS data[42]. Furthermore, there are insufficient reports on the systematic characterization of the optical properties of pristine NiO and Ni0.95 × 0.05O (X = Cr, Fe, Co, Cu, and Zn) nanopowders by the K-K analysis. Besides, as we know, optical parameters can be affected by structural and morphological characteristics such as shape and size.

Hence, in the present study, for the first time, a wide range of essential, crucial, and practical elements, including chromium, iron, cobalt, copper, and zinc, have been successfully doped into NiO under similar circumstances. Following the successful synthesis of the aforementioned nanopowders, their structural and morphological characteristics and the evaluation of the effect of these characteristics on optical parameters in terms of doping effect and calcination temperature have been investigated. The structural parameters of the samples were deduced from XRD data. Also, the elemental, functional, optical, and magnetic properties of nanoparticles were investigated based on energy dispersive X-ray spectroscopy (EDS), Fourier transform infrared spectroscopy (FTIR), diffuse reflectance spectroscopy (DRS) using (K-K) relations, and vibrating sample magnetometer (VSM). In addition, the monolayer adsorption volume (V_m), surface area, and average particle size (D_{BET}) of the prepared powders were analyzed using the Brunauer–Emmett–Teller (BET) method.

Experimental details

Preparation of NiO nanoparticles

The co-precipitation method has been used to synthesize nickel oxide and samples doped with chromium, iron, cobalt, copper, and zinc. All the chemicals employed in this study were reagents of analytical grade and were utilized without any additional purification. The used following precursor materials in this study were purchased from Merck company: Nickel (II) nitrate hexahydrate ($Ni(NO_3)_2.6H_2O$) (CAS#:13478-00-7), Chromium (III) nitrate nonahydrate ($Cr(NO_3)_3{\cdot}9H_2O$) (CAS#:7789-02-8), Cobalt nitrate hexahydrate ($Co(NO_2)_2.6H_2O$) (CAS#:10026-22-9), Zinc nitrate hexahydrate ($Zn(NO_3)_2.6H_2O$) (CAS#:10196-18-6), Copper nitrate trihydrate ($Cu(NO_3)_2{\cdot}3H_2O$) (CAS#:10031-43-3) and Iron (III) chloride hexahydrate ($FeCl_3{\cdot}6H_2O$) (CAS#:0250-03943-1). Supplementary Fig. 1 represents the synthesis process and the chemical reaction behind the formation of the synthesized nanoparticles. For synthesizing 0.5 M NiO nanoparticles, 14.54 gr of nickel nitrate hexahydrate [Ni (NO3)26H2O] was added to 100 ml distilled water and stirred in a beaker at 80 degrees for 30 min. Then, the Ammonia solution was slowly (in drops) added to form a green precipitate. Ammonia solution is used as a reduction agent. The resultant solution was stirred at the same temperature for 2 h, followed by multiple rinses with ethanol and water to attain a neutral pH of 7. To obtain NiO powder, the sediment of the final solution was dried and calcined at 600 degrees for 4 h. On the other hand, for preparation of doped samples, the Co-precipitation method was used as follows: a 100 cc amount of 0.5 M Nickel (II) nitrate hexahydrate solution is poured into a beaker and stirred for 30 min when it becomes uniform, Fe, Cu, Zn, Co and Cr (0.05w%) solution was added to it. After 30 min, 1 M NaOH solution was added to the final product drop by drop for 1 h. Then, it is stirred for 2 h at a temperature of 80 degrees until a precipitate is formed. The resultant precipitate is washed and dried in an oven for 16 h and calcined in the furnace. The calcination temperature of each dope was different: Fe: 850 ?, Cu: 550 ?, Co: 650 ?, Cr: 700 ?, and Zn: 700 ?[43–45].

Given that the treatment temperature can influence the crystal structure and size of nanoparticles during the synthesis process, and considering that the size, shape, and crystal structure of the particles affect the optical performance. In this study, to produce nanoparticles affected with a better optical performance and to remove moisture and convert hydroxide to metal oxide, testing, and optimization were conducted at a temperature of 500 to 850 ?. Within this range of temperatures, specific temperatures that exhibited appropriate optical behavior in nanoparticles were chosen to enable comparison of the resulting samples. Moreover, by optimizing the temperature during this process and considering the low doping percentages of the elements, the different doping was distinguished from one another. These temperatures are the usual ones used in previous works (Fe: 850 ℃, Cu: 550 ℃, Co: 650 ℃, Cr: 700 ℃, and Zn: 700 ℃)[46–51].

Characterization

The investigation of the structural characteristics of pristine and (Cr, Fe, Co, Cu, and Zn) doped NiO synthesized powders was conducted utilizing a high-resolution X-ray diffraction system (Philips PW 1730) provided with Cu-Kα radiation at a wavelength of λ = 0.154056 nm, from an angle of 2θ = 30°–80°. The analysis of the surface morphology was conducted using the FE-SEM) (TeScan-Mira III, Czech Republic) and ImageJ analysis software along with energy-dispersive X-ray spectrometry (EDAX) (SAMX, TeScan) for the determination of chemical composition and BET measured by BELSORP II (BEL JAPAN Inc.). The observation of vibrational modes of metal oxide bonds and the detection of functional groups were performed using Fourier-transform infrared spectroscopy (FTIR) (Thermo Scientific, Nicolet, Avatar, USA) and was carried out over a wavenumber range of 400–4000 cm^{-1}. The magnetic characteristics were assessed using a vibrating sample magnetometer (VSM-MDKB) in a 1.4 T field at room temperature. Finally, the optical evaluations were conducted using DRS (Sinco S4100 Korea) data and the Kramers-Kronig method through MATLAB coding.

XRD data were collected using X'pert Highscore Plus software with the following information:

(Version: 2.2b (2.2.2), Date: 01-11-2006). To calculate the size of prepared nanoparticles, of Digimizer software was used: (Version: 4.1.1.0, Copyright © 2005–2011 MedCalc Software). XRD, FTIR, EDX, VSM, and DRS data were plotted using the Origin scientific plotting program with the following information: (OriginPro 2018 (64-bit) SR1, b9.5.1.195).

Results and discussion

Structural investigations

Figure 1. demonstrates the XRD pattern of pristine and (Cr, Fe, Co, Cu, and Zn)-doped NiO powders synthesized using the co-precipitation method.

As shown in Fig. 1 (a), all the synthesized samples have a polycrystalline cubic structure. For both pristine and doped NiO samples, the diffraction peaks located at 37.37°, 43.41°, 62.98°, 75.51°, and 79.50° equal to the (111), (200), (220), (311), and (222) planes of the face-centered-cubic structure of nickel oxide, respectively. The obtained pattern aligns with the established pattern of NiO (JCPDS card No. 01-075-0197)[52,53]. The patterns derived from XRD did not display any secondary peaks indicative of the existence of impure or secondary phases such as Ni in metallic form, Ni_2O_3, Zn (metal or oxide), Fe oxides like Fe_2O_3, Fe_3O_4, or spinel phases like $NiFe_2O_4$, chromium or chromium compound, CoO, Co_2O_3 or Co_3O, and Cu_2O, elemental segregations at boundaries of the grains or clusters. This confirms the incorporation of all dopants into the NiO lattice. Furthermore, the position of the peaks, such as the most intense peaks, in the XRD pattern shifts towards lower and higher angles as doping into the NiO structure confirms the successful incorporation of dopants into the NiO lattice (Fig. 1 (b)). Due to the comparable ionic radius of Ni^{+2} (0.69 Å), Ni^{3+} (0.60 Å), Cr^{3+} (0.615 Å), Fe^{+2} (0.74 Å), Fe^{+3} (0.64 Å), Co (0.74 Å), Cu^{+} (0.77 Å), Cu^{2+} (0.73 Å), Zn^{2+} (0.74 Å), Since the disparity in ionic radii among Ni^{+2}, Ni^{3+}, and aforementioned dopants is small and negligible, it is feasible for dopants to substitute Ni^{+2}, Ni^{3+} ions without infringing upon the lattice structure[23,54]. The dislocation density, crystallite size, lattice parameter, lattice micro-strain, and interplanar spacing value of the synthesized samples as important structural parameters are evaluated based on the most intense XRD peak and tabulated in Table 1. The lattice parameters are obtained using Eq. (1)[55].

$$a_{hkl} = d_{hkl}\sqrt{h^2 + k^2 + l^2} \tag{1}$$

Here, *d* represents the value of the interplanar spacing, which is calculated using the given equation:

$$n\lambda \ = 2dsin? \tag{2}$$

a_{hkl} denotes the parameter of the lattice (for cubic, $c = b = a$), and *h*, *k*, and *l* represent the Miller indices.

The crystallite size of the synthesized powders *(D)* is determined using the most intense peak in the X-ray diffraction (XRD) patterns, applying the Debye-Scherrer equation. This relation is defined as follows[56,57]:

$$D = \frac{k\lambda}{\beta\,{}^{1}/_{2}\,cos\theta} \tag{3}$$

where λ represents the wavelength of copper (λ = 0.15406 nm), *K* is a constant value of 0.9, θ is the diffraction angle, and β is the width of the peak.

In addition, dislocation density (denoted by δ) and lattice micro-strain (denoted by ε) are calculated through Eqs. 4 and 5, respectively[58,59].

$$\delta \ = \frac{1}{D^2} \tag{4}$$

$$\epsilon \ = \frac{\beta\,{}^{1}/_{2}}{4\,tan\theta} \tag{5}$$

The parameter δ, which characterizes the presence of imperfections, exhibits an inverse proportionality to the square of the size of the crystallites. Expressly, it signifies the proportion of the dislocation lines' extent encompassed within a unit cell of a nanoscale material to the volume of the crystalline structure.

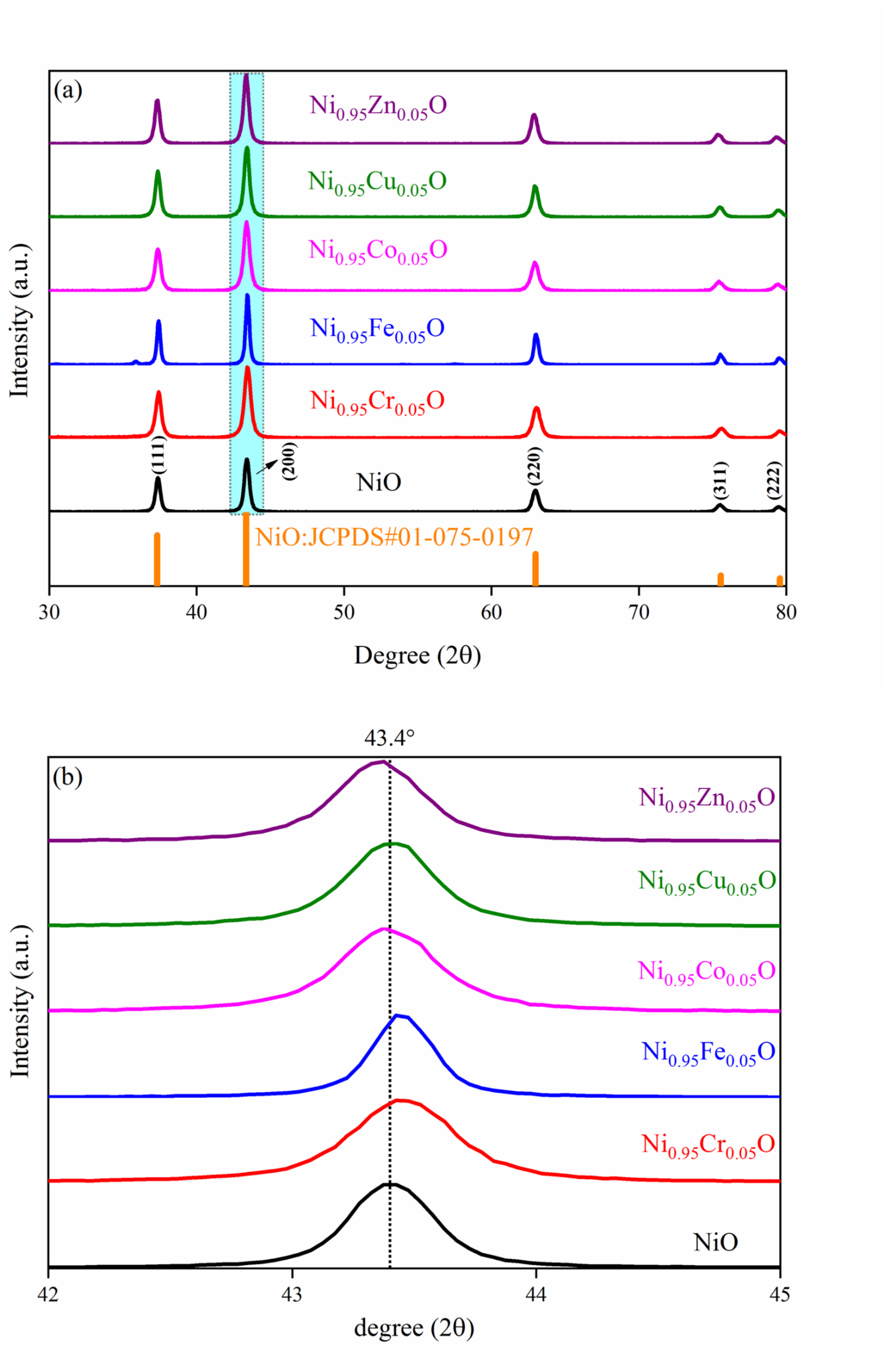

Fig. 1. **a** XRD patterns of pristine and (Cr, Fe, Co, Cu, and Zn)-doped NiO powders, **b** enlarged version of corresponding samples at miller indices (200)

The data in Table 1 demonstrates that the doping of (Cr, Co, Cu, and Zn) results in an increase in dislocation density and a decrease in Fe-doped NiO. The replacement of (Cr, Co, Cu, and Zn) in the NiO lattice leads to an increase in vacancies and defects, as evidenced by the increase in dislocation density. The significantly higher ε and δ values observed in the chromium-doped NiO sample (as outlined in Table 1) confirm the presence of more substantial crystal imperfections or structural disorder. This disorder leads to smaller dimensions of the crystallites and a reduction in crystallinity. Table 1 reveals that the crystallite dimensions of the pristine nickel

Samples/parameters	2θ (°)	(a = b = c) (Å)	d (Å)	FWHM	ϵ	D (nm)	δ ($\times$ 10^{14}line/m^2)
NiO	43.41	4.17	2.083	0.4399	0.0048	20.29	24.29
$Ni_{0.95}Cr_{0.05}O$	43.45	4.16	2.081	0.5482	0.0060	16.29	37.68
$Ni_{0.95}Fe_{0.05}O$	43.45	4.16	2.081	0.3212	0.0035	27.80	12.94
$Ni_{0.95}Co_{0.05}O$	43.39	4.17	2.084	0.5274	0.0058	16.93	34.89
$Ni_{0.95}Cu_{0.05}O$	43.40	4.17	2.083	0.4675	0.0051	19.09	27.44
$Ni_{0.95}Zn_{0.05}O$	43.36	4.17	2.085	0.4694	0.0052	19.02	27.64

Table 1. Structural parameters of the prepared powders from (200) diffraction

oxide increase with Fe doping. The slight changes in lattice parameters are attributed to the variations in ionic radii. The density of dislocations pertains to the number of lattice imperfections in the material. The occupation of interstitial sites may cause an expansion in lattice parameters. On the other hand, in the doped samples, the oxidation of Ni^{2+} to Ni^{3+} or the oxygen vacancies may lead to a change in the lattice constant. This is due to the smaller radius occupied by oxygen vacancies relative to lattice oxygen and the smaller ionic radius of Ni^{3+} compared to Ni^{2+}. Reduced dimensions of crystallites exhibit enhanced lattice defects and increased influences of grain boundaries, as evidenced by the calculated δ through Eq. 4 presented in Table 1[60,61]. Furthermore, the broadening of the peaks is exacerbated by various doping elements, which suggests a reduction in the size of the crystallites, except for iron doping, which was estimated using the Scherrer formula. The values of the lattice parameters (a) are significantly influenced by doping[62,63].

Morphological studies

Morphological studies, including surface morphology and grain size of pristine and doped NiO powders, were conducted using FE-SEM, as depicted in Fig. 2 (a-f). In all synthesized samples, observations reveal minimal agglomeration, a random and homogeneous distribution, and roughly spherical grains, along with the absence of defects and superior crystal quality[64]. This agglomeration results from the nano-scale dimensions of the crystal size, whereby nanocrystals possess a significant amount of surface energy[65]. Furthermore, the aggregation of metal oxide nanoparticles is a compensation mechanism for the surface energy resulting from the high surface-to-volume proportion. Additionally, this random distribution results from the site selection of dopant ions on the surface of host materials. On the other hand, doped NiO powders exhibit well-distributed and uniform grains. The growth and nucleation process of NiO is impacted by the presence of dopants, which subsequently affects the morphology and size of the samples. The dissymmetry in crystallite size may be attributed to the fusion of different crystallites, resulting in the formation of polycrystalline grains[66]. The incorporation of Cr, Cu, Zn, and Co ions into NiO leads to a reduction in grain size, indicating an increase in strain within the lattice and a restriction in its growth. Additionally, Fig. 3 (a-f) displays the size distribution histograms of the prepared powders computed and plotted with the help of Digimizer software[67]. All synthesized samples exist in the nanoscale with a mean size range of (63–109 nm). This observation aligns with the crystallite dimensions revealed through XRD. As seen in Table 1, the reduction of the interplanar distance (d) in nanoparticles leads to a decrease in the crystal dimensions (a = b = c) and an increase in the size of the crystallites[68]. On the other hand, with the increase in the size of the crystallites, the diameter of the nanoparticles (which are the result of the joining of several crystallites) observed in the FE-SEM shapes also increases[69]. As a result, the agreement between XRD and FE-SEM results is confirmed for the samples under study.

Finally, static volumetric adsorption studies, including s specific surface area and pore parameters of pristine and doped NiO powders, were depicted in Fig. 4 (a-f). The specific surface area of pure and (Cr, Fe, Co, Cu, and Zn) doped NiO nanopowders calculated using the multipoint BET-equation[70] are 22.841, 37.331, 16.404, 42.197, 32.466 and 29.940 m^2/g respectively. Table 2 presents the BET experimental results of pure and (Cr, Fe, Co, Cu, and Zn) doped NiO.

It is important to note that the effect of agglomeration (SEM analysis) on both crystallites (XRD analysis) and surface area (BET analysis) values can vary depending on the material, the agglomeration process, and the specific measurement technique that crystallites constitute the diffraction domain[71].

Elemental evaluations

The compositional analysis of pristine and doped NiO nanoparticles was conducted through EDS, and the obtained spectra are depicted in Fig. 5 (a-f). As can be seen, the pristine NiO nanoparticles confirm the presence of elementary species such as nickel and oxygen. In addition to nickel and oxygen, doped elements such as zinc, cobalt, chromium, copper, and iron can also be observed in the doped samples. The absence of additional materials indicates the preservation of the phase integrity in the nano-sized structures. The EDS analysis demonstrated distinct peaks solely for the Ni, O, and related doping elements, with no detection of any supplementary peaks. This indicates that the powder prepared in its original state is free from impurities, confirming the appropriate incorporation of dopants within the NiO matrix.

Functional investigations

The Fourier Transform Infrared (FTIR) spectra provide valuable insights into various aspects of bonds, including modes of vibrations (stretching and bending) and vibrational frequencies. Furthermore, it offers valuable

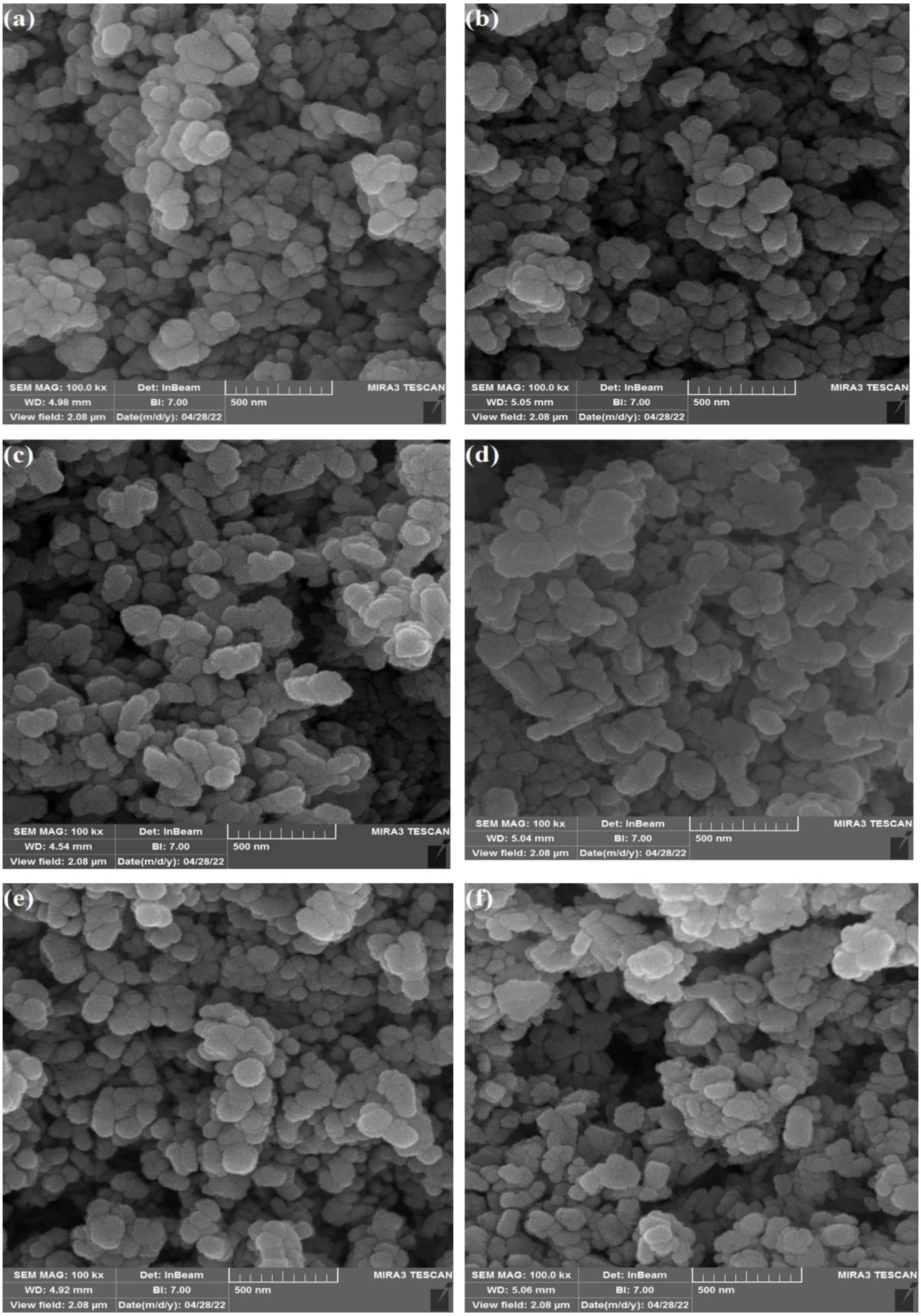

Fig. 2. FESEM images of the prepared powders: **a** NiO; **b** $Ni_{0.95}Cr_{0.05}O$; **c** $Ni_{0.95}Fe_{0.05}O$; **d** $Ni_{0.95}Co_{0.05}O$; **e** $Ni_{0.95}Cu_{0.05}O$; **f** $Ni_{0.95}Zn_{0.05}O$

information about the molecular interactions within the synthesized nanoparticles. Figure 6 presents the FTIR spectra of the synthesized pristine and doped NiO nanopowders, spanning the spectral area of 400–4000 cm^{-1}. The distinct peaks of metal hydroxide (M-OH) framework bonds and metal-oxygen (M-O) are prominently displayed in the lower wavenumber region (400–700 cm^{-1})[45]. The broad spectral range in all synthesized samples, with its focal point at approximately 416–528 cm^{-1}, is concrete evidence supporting the creation of the crystalline NiO nanoparticles and not the bulk NiO[72]. This specific spectral range can be attributed to the

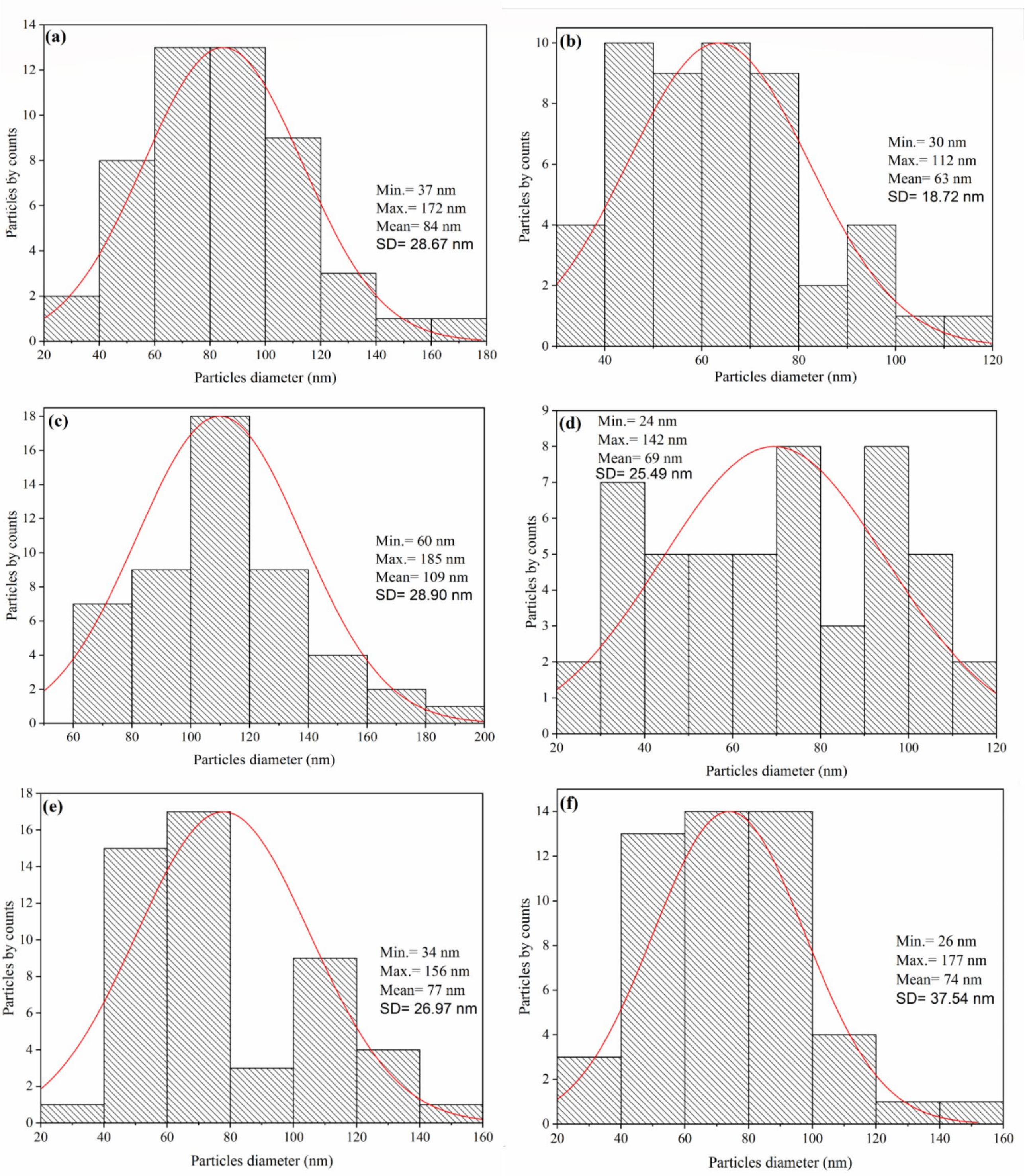

Fig. 3. Histogram of the size distribution of the prepared samples: **a** NiO; **b** $Ni_{0.95}Cr_{0.05}O$; **c** $Ni_{0.95}Fe_{0.05}O$; **d** $Ni_{0.95}Co_{0.05}O$; **e** $Ni_{0.95}Cu_{0.05}O$; **f** $Ni_{0.95}Zn_{0.05}O$

vibration from the Ni-O stretching[73]. It has been noted that the peaks of Ni-O stretching vibrations undergo a slight displacement in the presence of various doping[74]. Unit cell volume, nanoparticles' geometry, quantum size effect, and Non-stoichiometry have been documented as factors contributing to peak shifting[52,75]. Furthermore, the confirmation of the existence of C-O in the initial substance is validated by the occurrence of a peak at approximately 786 cm^{-1} and 1035 cm^{-1}. The detected vibration modes resulted from alternative chemical bonding, precisely the stretching vibrations of C-O at 1035 cm^{-1} due to air[76]. The peak at 1384 cm^{-1} indicates the symmetrical stretching bond and is attributed to the bending vibration of the ionic carbonate species. This

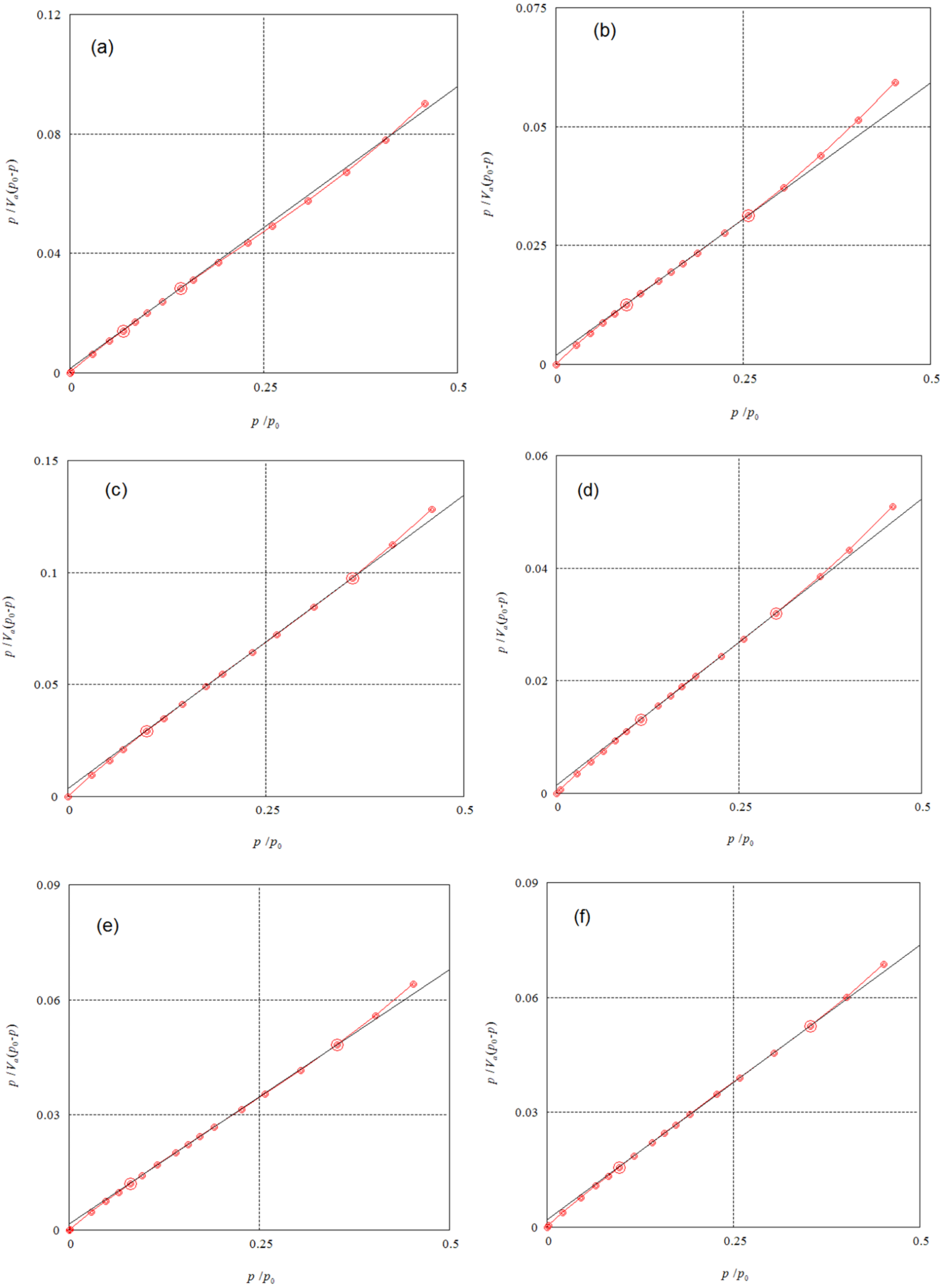

Fig. 4. BET plots of prepared powders: **a** NiO; **b** $Ni_{0.95}Cr_{0.05}O$; **c** $Ni_{0.95}Fe_{0.05}O$; **d** $Ni_{0.95}Co_{0.05}O$; **e** $Ni_{0.95}Cu_{0.05}O$; **f** $Ni_{0.95}Zn_{0.05}O$

particular peak signifies the absorption of carbon dioxide from the surrounding atmosphere onto the surface of nickel oxide[77] and shows the vibrations of NO^{-3}[78]. The spectral peak at 1628 cm^{-1} is attributed to the bending vibrational mode of the physisorption of H_2O on the surface of the prepared nanopowders. This phenomenon occurs due to water adsorbed in the air during the preparation process in an open atmosphere. Additionally, the stretching vibrations of the hydroxide are responsible for the widely observed absorption peak at approximately 3447 cm^{-1}[79]. These peaks at 1628 cm^{-1} and 3447 cm^{-1} are ascribed to the bending of O–H bonds and the

Sample	Constant C	Monolayer adsorption volume V_m	BET surface area S_{BET}	Average particle Size D_{BET}
NiO	145.38	5.2478 $^{cm^3}/_{g}$	22.841 $^{m^2}/_{g}$	63 nm
$Ni_{0.95}Cr_{0.05}O$	61.746	8.5770 $^{cm^3}/_{g}$	37.331 $^{m^2}/_{g}$	47 nm
$Ni_{0.95}Fe_{0.05}O$	77.693	3.7690 $^{cm^3}/_{g}$	16.404 $^{m^2}/_{g}$	42 nm
$Ni_{0.95}Co_{0.05}O$	71.932	9.6950 $^{cm^3}/_{g}$	42.197 $^{m^2}/_{g}$	36 nm
$Ni_{0.95}Cu_{0.05}O$	84.660	7.4591 $^{cm^3}/_{g}$	32.466 $^{m^2}/_{g}$	52 nm
$Ni_{0.95}Zn_{0.05}O$	71.932	6.8790 $^{cm^3}/_{g}$	29.940 $^{m^2}/_{g}$	49 nm

Table 2. BET experimental results of the prepared powders: (a) NiO; (b) $Ni_{0.95}Cr_{0.05}O$; (c) $Ni_{0.95}Fe_{0.05}O$; (d) $Ni_{0.95}Co_{0.05}O$; (e) $Ni_{0.95}Cu_{0.05}O$; (f) $Ni_{0.95}Zn_{0.05}O$

stretching of hydroxyl (O–H) bonds, respectively[80]. Also, the weak band 2923 cm^{-1} is attributed to the C-H stretch. Table 3 represents the FT-IR spectral bands of the synthesized samples. No additional notable peaks are detected for any contaminants or secondary phases in the spectra, thereby corroborating the elevated purity of the prepared nanopowders. This observation indicates that dopants are uniformly distributed within the supporting matrix. It is crucial to acknowledge that the positions and intensities of the FTIR bands may fluctuate based on several variables, such as crystallite size, the type of dopants, and the methodology of fabrication. Nevertheless, the FTIR bands identified yield significant insights into the functional groups and chemical bonding in the pristine and doped NiO nanopowders[81,82]. These findings illustrate that the samples that were prepared exhibit no indications of contamination, a phenomenon that aligns with the XRD findings.

Magnetic measurements

The examination of the magnetic characteristics of the synthesized samples was conducted under atmosphere conditions. The magnetization's intensity was enhanced due to the external magnetic field being applied, reaching a maximum of ±15 kOe. These findings are depicted in Fig. 7. Furthermore, the coercivity (Hc), remanence (Mr), and saturation magnetization (Ms) values for the samples are exhibited in Table 4. NiO displays antiferromagnetism (AFM) characteristics in its bulk state. In contrast, when it is scaled down to the nanometer level, it can demonstrate remarkable magnetic characteristics owing to the existence of a surface magnetization and ferromagnetic nickel phase it hence can exhibit different magnetic properties such as superparamagnetism (SPM), ferromagnetism (FM), and spin glass behavior can be observed[83]. It has been noted that at the nanoscale, broken symmetry, exchange restrictions, and broken bonds contribute to unique magnetic characteristics. Furthermore, oscillations in the lattice affect the superexchange interactions, including the bond length and angles that could result in weak FM[84]. The mechanism responsible for the emergence of FM at ambient temperature in antiferromagnetism nickel oxide is still a subject of controversy. The vacancy-induced ferromagnetism for antiferromagnetism nickel oxide nanopowders is the commonly used mechanism, and the ferromagnetism interaction was correlated with the presence of both Ni^{2+} vacancies and uncompensated surface O^{2-}[85]. Besides, FM is a result of the degradation of long-range AFM exchange. The findings indicate that the saturation magnetization (Ms) of the synthesized nickel oxide nanoparticles is significantly lower than bulk nickel. The obtained coercivity (Hc) values in this study are consistent with the literature[86]. Conversely, the Hc values exhibit higher values than the bulk coercivity. The coercivity value at room temperature has been determined to exceed the analogous value for bulk nickel, with Hc = 100 Oe[87,88]. These values also confirm the superior magnetic properties of the NiO nanoparticles compared to nickel microstructures. This augmentation in coercivity can be attributed to the reduced particle size[89]. It has come to light that the coercivity can be modified due to dipolar interactions and exchange resulting from an increase in the energy barrier[90]. As can be seen from Fig. 7 (a-c), all the synthesized samples demonstrated an FM nature. Importantly, the FM nature of NiO nanoparticles arises from the existence of Ni (III) ions or SPM metallic Ni (0) as traces in the NiO sample. The pristine NiO exhibits a weak FM signal, with a Ms equal to 0.276 emu/g, which can primarily be attributed to the cationic vacancies of Ni^{2+} in the octahedral site[91]. This disturbance affects the superexchange interaction between $Ni^{2+}–O^{2-}–Ni^{2+}$. The magnetic and physical characteristics significantly rely on the preparation conditions. Numerous intrinsic and extrinsic factors alter the magnetic states, such as the interaction between the magnetic moments, the presence of induced surface vacancy defects, site occupation, concentration, crystal morphology, and structure, the finite size effect, the existence of secondary phases, and the method of synthesis[80,92]. Moreover, the introduction of doping leads to a change in particle size, which can potentially result in the creation of metal vacancies[93]. The substitution of zinc (Zn), copper (Cu), cobalt (Co), iron (Fe), or chromium (Cr) in the NiO matrix gives rise to three possibilities: (i) substitution at both the core and surface of NiO, (ii) substitution only at the surface of NiO, and (iii) substitution solely in the core of NiO. If dopants are substituted at the surface of NiO, the magnetic moment decreases because of the nonmagnetic characteristics of the dopants. Consequently, weak FM emerges alongside the AFM nickel oxide, resulting in a higher magnetization than pure NiO. If dopants are incorporated in the core, the antiferromagnetism superexchange interaction could be disrupted. In our study, since both the a)

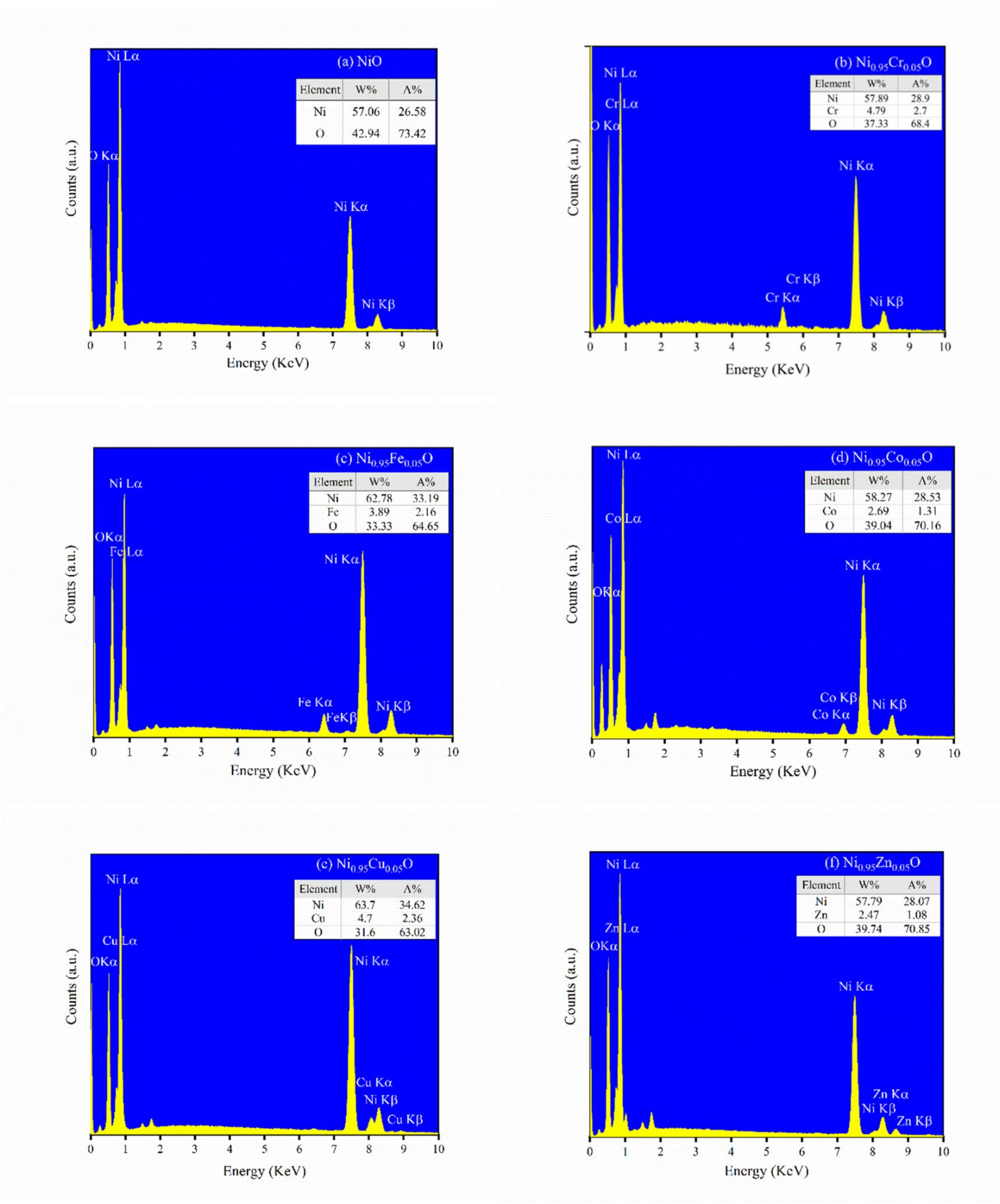

(a) NiO

Element	W%	A%
Ni	57.06	26.58
O	42.94	73.42

(b) $Ni_{0.95}Cr_{0.05}O$

Element	W%	A%
Ni	57.89	28.9
Cr	4.79	2.7
O	37.33	68.4

(c) $Ni_{0.95}Fe_{0.05}O$

Element	W%	A%
Ni	62.78	33.19
Fe	3.89	2.16
O	33.33	64.65

(d) $Ni_{0.95}Co_{0.05}O$

Element	W%	A%
Ni	58.27	28.53
Co	2.69	1.31
O	39.04	70.16

(e) $Ni_{0.95}Cu_{0.05}O$

Element	W%	A%
Ni	63.7	34.62
Cu	4.7	2.36
O	31.6	63.02

(f) $Ni_{0.95}Zn_{0.05}O$

Element	W%	A%
Ni	57.79	28.07
Zn	2.47	1.08
O	39.74	70.85

Fig. 5. EDS spectra of the prepared samples: **a** NiO; **b** $Ni_{0.95}Cr_{0.05}O$; **c** $Ni_{0.95}Fe_{0.05}O$; **d** $Ni_{0.95}Co_{0.05}O$; **e** $Ni_{0.95}Cu_{0.05}O$; **f** $Ni_{0.95}Zn_{0.05}O$.

remanent magnetization (Mr) and coercivity (Hc) values decrease with doping, we infer that agglomeration leads to an increase in effective particle size. Conversely, when both the Mr and Hc parameters increase with doping, a certain amount of dopants substitute at the Ni sites in the core along with the surface substitution, thereby improving its magnetic properties[91]. Moreover, Ms lower amounts for (Cu, Cr, and Zn)-doped NiO samples, compared to pristine NiO, can be associated with a reduced contribution of oxygen vacancy. In all samples room-temperature ferromagnetism (RTFM) could be attributed to the double exchange interactions

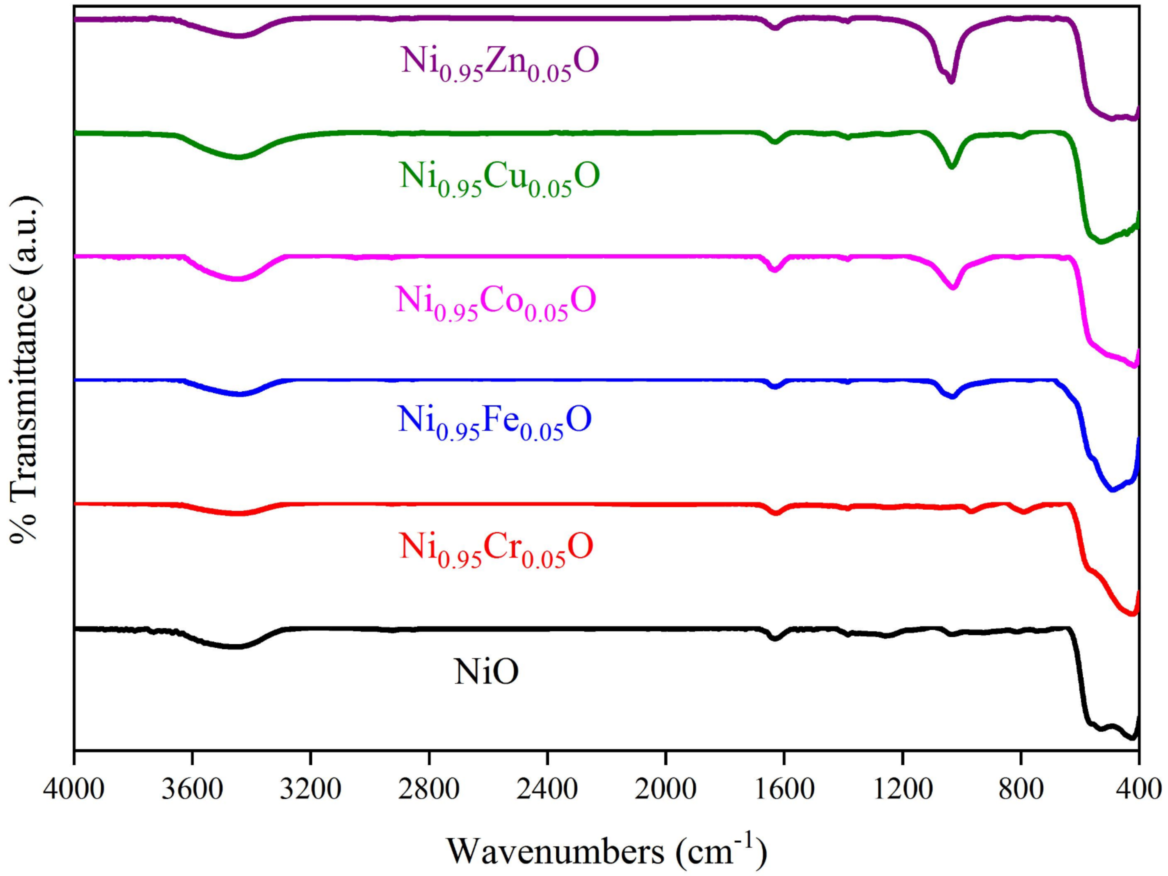

Fig. 6. FT-IR spectra of the prepared samples

Samples	Assignments			
	Ni-O stretching	C-O	O-H bending	O-H stretching
NiO	424 cm^{-1}	1034^{-1}	1630 cm^{-1}	3454 cm^{-1}
$Ni_{0.95}Cr_{0.05}O$	423 cm^{-1}	980^{-1}	1627 cm^{-1}	3443 cm^{-1}
$Ni_{0.95}Fe_{0.05}O$	489 cm^{-1}	1031^{-1}	1629 cm^{-1}	3438 cm^{-1}
$Ni_{0.95}Co_{0.05}O$	416 cm^{-1}	1028^{-1}	1629 cm^{-1}	3444 cm^{-1}
$Ni_{0.95}Cu_{0.05}O$	528 cm^{-1}	1032^{-1}	1629 cm^{-1}	3442 cm^{-1}
$Ni_{0.95}Zn_{0.05}O$	421 cm^{-1}	1035^{-1}	1630 cm^{-1}	3440 cm^{-1}

Table 3. FT-IR spectral bands (cm^{-1})

among the defects and induced magnetic Cr, Fe, Co, Cu, and Zn ions. The presence of RTFM in Cu-doped NiO suggests that, there is a relation between the superexchange coupling and F-centre exchange coupling[94]. The FM condition observed in copper-doped nanoparticles can be attributed to the substitution of Cu^{2+} for Ni^{2+} and the substantial oxygen vacancies[95]. Substitution of Fe in the NiO engenders charge carriers, thereby leading to an increased exchange interaction and resulting in a higher Ms. The observed hysteresis in the Fe-doped sample aligns with previous findings because of the uncompensated spins; the curve gradually narrows[32,96]. The magnetic characteristics of the nanopowders are highly linked to their crystallinity, magnetic direction, shape, and particle size. In addition, Fe-doped NiO nanoparticles displayed an enhanced saturation magnetization value and demonstrated evident FM properties at room temperature due to the substitution of Fe in the NiO lattices. Based on our findings, we can rule out the segregation of iron as the source of FM in the prepared Fe-doped NiO, indicating intrinsic FM properties[97]. Thus, double exchange interactions are enhanced through iron doping, resulting in a higher magnetic moment[98]. As a result, Fe-doping disrupts the magnetic ordering of NiO and gives rise to FM through a double exchange system[99]. The substitution of Zn^{2+} ions for Ni^{2+} ions within the NiO matrix can occur both at the surface and the core of the material. Consequently, a localized weak FM

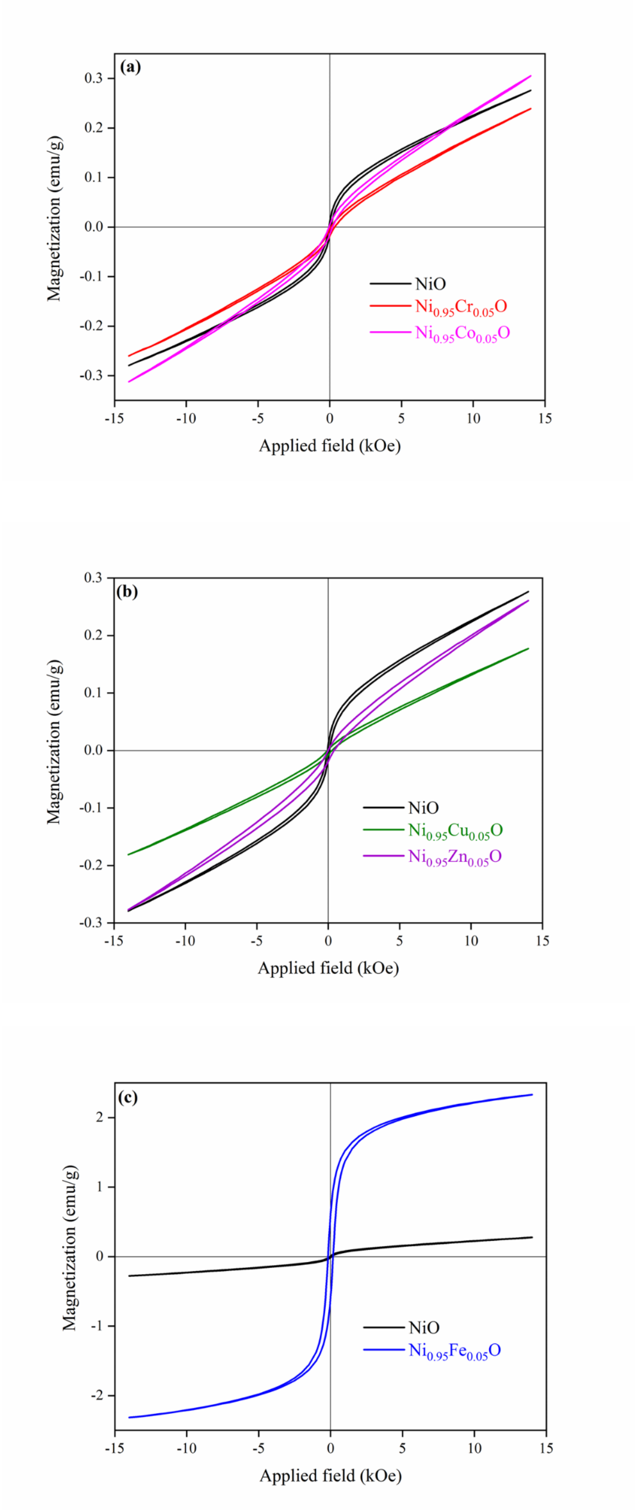

Fig. 7. Comparing M – H curves of the prepared samples: **a** NiO, $Ni_{0.95}Cr_{0.05}O$, and $Ni_{0.95}Co_{0.05}O$; **b** NiO, $Ni_{0.95}Cu_{0.05}O$, and $Ni_{0.95}Zn_{0.05}O$; **c** NiO, and $Ni_{0.95}Fe_{0.05}O$

ordering is generated within the background of the NiO sample[26]. The magnetization in NiO is caused by the substitution of the Co with unpaired electrons in its d shell for the cation site of Ni. The Co-doped nanopowder exhibits an enhancement in magnetic characteristics, which can be associated with the cobalt's high magnetic moment and its FM properties[100]. Overall, the magnetic properties of NiO were significantly enhanced through Co^{2+} doping. The Ms improvement in the Co-doped NiO sample can be attributed to the higher magnetism exhibited by Co^{2+} compared to Ni^{2+}[101].

Sample	M_r (emu/g)	M_s (emu/g)	H_c (Oe)	Loop Area (Oe × emu/g)	SQR
NiO	0.010	0.276	80.4390	131.489	0.036
$Ni_{0.95}Cr_{0.05}O$	0.001	0.239	246.836	111.255	0.004
$Ni_{0.95}Fe_{0.05}O$	0.605	2.331	174.775	1509.69	0.260
$Ni_{0.95}Co_{0.05}O$	0.004	0.305	182.329	176.112	0.013
$Ni_{0.95}Cu_{0.05}O$	0.001	0.177	249.517	110.541	0.006
$Ni_{0.95}Zn_{0.05}O$	0.040	0.260	350.746	241.295	0.154

Table 4. The magnetic parameters for the synthesized samples

To determine the nature of domains and the squareness of the hysteresis loop, the squareness ratio (SQR) derived from the M-H curve was computed and recorded in Table 4. SQR is the ratio of Mr to Ms, SQR = Mr/Ms (6)[102]. All obtained SQR values are below 0.5, confirming the multidomain structure of the nanostructures and indicating that the magnetic interactions are associated with grains or particles within the nanoparticles[83,103]. The SQR value for Fe-doped NiO is 0.260, which makes it suitable for applications in data storage as well as a magnetic soft material for battery cathodes and transformers[90]. Coercivity and remanence are supplemented by metrics that characterize the geometric shape of the hysteresis loop and the corresponding area encompassed within loop[104]. The cumulative area of the hysteresis loop derived from the M(H) data constitutes a significant parameter that influences the dissipation of magnetic energy attributable to irreversible movements of domain walls and the rotation of domains within the material[105]. The area of the hysteresis loop represents the necessary energy for completing a cycle involving both demagnetization and magnetization while simultaneously indicating the energy losses incurred throughout this process[106]. In other words, the area of the hysteresis loop acts as an indicator of magnetostatic energy dissipation resulting from the dynamics of domain wall displacement and rotation[107]. The XRD analysis supports the rationale behind the ferromagnetism of NiO nanoparticles. The observed RTFM, characterized by a face-centered cubic structure, plays a crucial role in integrated microelectronic devices and spintronics[108].

Optical properties

Reflectance and band gap

The reflectance spectra of the prepared nanopowders are presented in Fig. 8 (a). This Figure shows the reflectance (%R) measured at ambient temperature as a function of wavelength for the synthesized nanopowders via the co-precipitation route. In general, the reflectance spectra of all synthesized samples increase as the wavelength increases. Compared to other synthesized samples, the reflectance spectrum of Fe-doped NiO is superior at the beginning of the near-infrared and end of the visible region. In contrast, the Zn-doped NiO exhibits higher reflectance spectra in the visible area. In most instances, a decrease in the mean coordination leads to smaller crystallite sizes and lower reflectance amounts. The decrease in reflectance is correlated with an increment in microstrain, dislocation density, crystal imperfections, and disorders[58]. The following statement about the band gap and the value of (n) is discussed and highlighted in the revised manuscript as follows:

In order to calculate the band gap (E_g) of semiconductor nanoparticles, the Kubelka–Munk function ($F\left(R\right)$) is used by absorption spectra from DRS data that is defined as the following relation[109]:

$$F\left(R\right)=\frac{(1-R)^2}{2R}=\frac{K}{S}\propto\ \alpha \tag{6}$$

where K and S are known as Kubelka-Munk absorption and scattering coefficients. Which $F\left(R\right)$ is the Kubelka – Munk function; $R=\left(R_{sample}\middle/R_{refrence}\right)$ is the diffuse reflectance ratio between the reference and sample. The band gap energy can be assessed by the following relationship between the Tauc relation and *F(R)* (Kubelka–Munk function)[110]:

$$F\left(R\right)hv=A(hv-E_g)^{1/n} \tag{7}$$

In which A is the proportionality constant that describes the degree of disorder in the sample, hv is the incident photon energy, and E_g is the band gap energy of the semiconductor. The value of n is related to the nature of electronic transition; it can take the values of 2, 1/2, 3 and 3/2 for direct allowed, indirect allowed, direct forbidden and indirect forbidden transitions, respectively[111]. Also, the E_g can be estimated with the Tauc plot method by plotting $(F(R)\ hv)^2$ in terms of the photon energy (hv) and extrapolating the liner part of the plot.

Figure 8 (b) illustrates the determination of the Energy band gap. The obtained results are summarized in Table 5. Zn doping leads to a blue shift, while other samples demonstrate a red shift. The band gaps for pristine and Cr, Fe, Co, Cu, and Zn–doped NiO are determined to be 3.41 eV, 3.07 eV, 3.17 eV, 3.33 eV, 2.77 eV, 3.46 eV, respectively, which is consistent with previous studies[19,20,30,55,79,108,112–114]. The variations in band gap values observed in different works could be attributed to differences in nanoparticle size. The addition of dopants in the NiO nanopowder enables the band gap engineering without causing any structural distortion. Therefore, the doped NiO samples exhibit great potential as a material for developing optoelectronic devices. As a result, the calculated bandgap energies are influenced by various factors, including impurity defects, lattice strain, oxygen vacancies, and crystallite size.

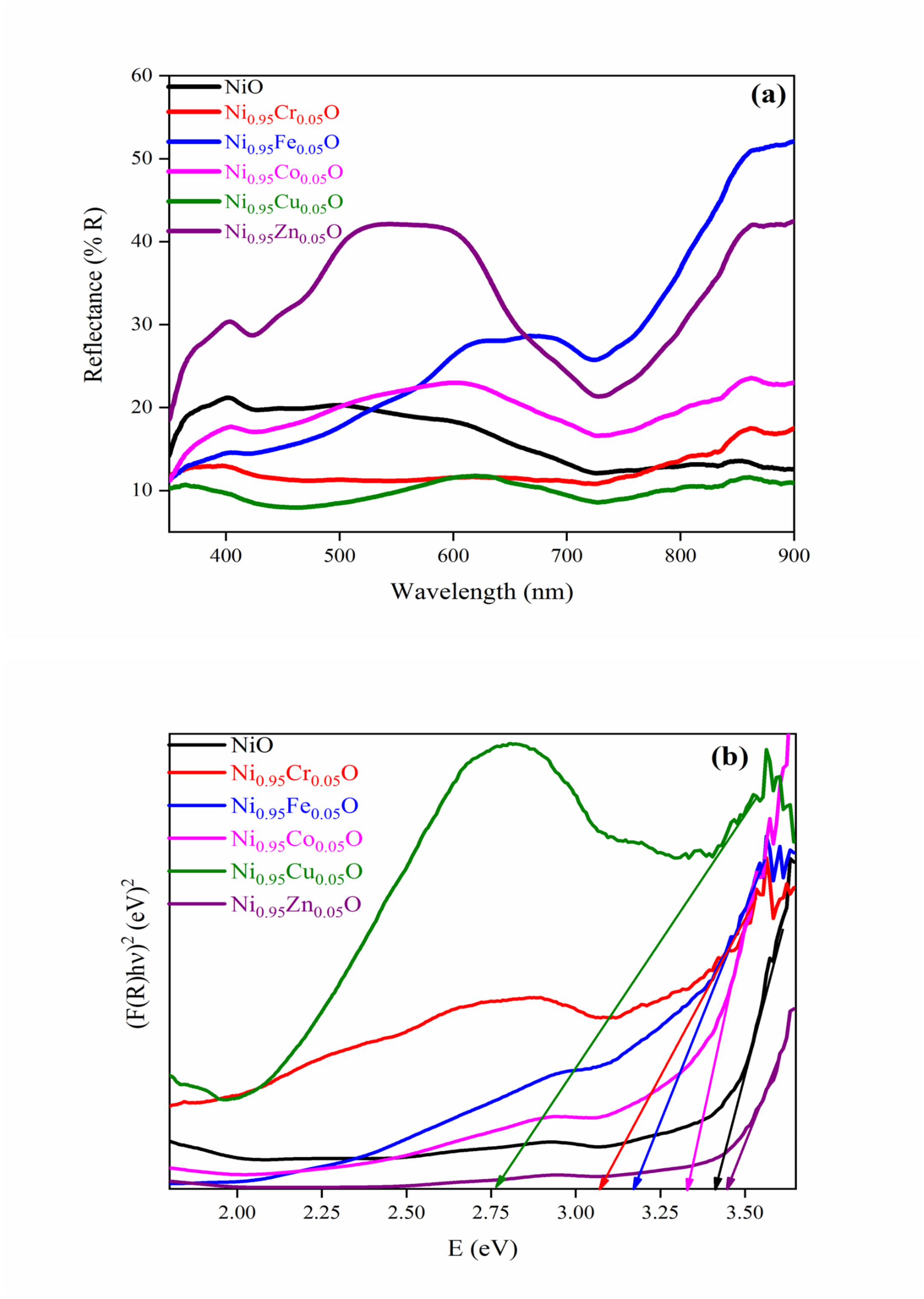

Fig. 8. **a** Reflectance spectra of the prepared nanopowders; **b** determination of the Energy band gap for the nanopowders.

Kramers–Kronig calculations

In the current study, we have calculated the optical constants of the nanopowders via MATLAB coding by employing reflectance values on the Kramers-Kronig technique[115]. The complex refractive index is represented as follows:

$$n^*(\omega) = n(\omega) + ik(\omega) \tag{8}$$

Sample	*R* (%)	E_g (eV)	*n*	k
NiO	21 (400 nm)	3.41	2.6	1.1
$Ni_{0.95}Cr_{0.05}O$	18 (860 nm)	3.07	2.0	0.8
$Ni_{0.95}Fe_{0.05}O$	52 (890 nm)	3.17	2.5	1.3
$Ni_{0.95}Co_{0.05}O$	24 (860 nm), 23 (607 nm)	3.33	2.7	1.2
$Ni_{0.95}Cu_{0.05}O$	12 (616 nm)	2.77	1.9	0.8
$Ni_{0.95}Zn_{0.05}O$	42 (890 nm, 540 nm)	3.46	4.4	2.2

Table 5. The obtained maximum reflectance (R%), band gap energies E_g (eV), maximum extinction coefficient (k), and refractive index (n) values for the nanopowders

k denotes the extinction coefficient, and *n* denotes the refractive index and can be given by:

$$k\,(\omega\,) = \left(\frac{2\sqrt{R(\omega\,)}sin\phi\,(\omega\,)}{1+R(\omega\,)-2\sqrt{R(\omega\,)}cos\phi\,(\omega\,)}\right) \tag{9}$$

$$n\,(\omega\,) = \left(\frac{1-R(\omega\,)}{1+R(\omega\,)-2\sqrt{R(\omega\,)}cos\phi\,(\omega\,)}\right) \tag{10}$$

φ(ω) is the phase angle and can be calculated via Kramers-Kronig dispersion as follows[42]:

$$\phi\,\,(\omega\,) = \left(\frac{\omega}{\pi}\right)\int\limits_0^\infty \frac{lnR\left(\omega\,'\,\right)-lnR(\omega\,)}{\omega\,'^{\,2}-\omega^{\,2}}d\omega\,' \tag{11}$$

$$\phi\,\,(\omega\,_i) = \left(\frac{4\omega\,_i}{\pi}\right)\times\,\Delta\,\omega\,\times\,\sum\,_i\frac{\ln\sqrt{R(\omega\,)}}{\omega\,'^{\,2}_i-\omega\,'^{\,2}_j} \tag{12}$$

$$\Delta\,\omega\,\,=\omega\,_{j+1}-\omega\,_j\left\{\begin{array}{ll} i=2.4.6.\ldots.j-1.j+1.\ldots & for\;odd\;j \\ i=1.3.5.\ldots.j-1.j+1.\ldots & for\;even\;j \end{array}\right. \tag{13}$$

k depending on the absorption of light and represents the imaginary component that is an indispensable parameter in optical devices. On the other hand, n represents the ability to stop the flow of electrons and signifies the actual component. Also, it is a vital parameter in optical applications such as switches, and optical modulation. The values of k and n at various wavelengths are depicted in Fig. 9. It can be observed that n exhibits higher amounts in the 460 nm < λ < 550 nm, after which it undergoes a sharp decline in the 290 nm < λ < 400 nm. The n for Zn-doped NiO varies widely from 1 to 4.5. Furthermore, a decrease in the amounts of n was caused by primary band gap absorption. The more minor n amounts are employed as an efficient medium in optical applications, such as those involving modifications in desired conductivity and mobility.

Moreover, it was noted that the values of k display abrupt rises and attain zero in the wavelength span of 450–560 nm, thus allowing the incident light to pass with minimal loss. The top amounts of k and n are listed in Table 5.

Conclusions

In conclusion, for both pure and doped nickel oxide (NiO) samples, the diffraction peaks identified at 37.37°, 43.41°, 62.98°, 75.51°, and 79.50° correspond to the (111), (200), (220), (311), and (222) planes of the face-centered cubic structure characteristic of nickel oxide, respectively. The patterns of the synthesized nanopowders verify the JCPDS card No. 01-075-0197 for all samples. The crystallite sizes were determined to be 20.29 nm, 16.29 nm, 27.80 nm, 16.93 nm, 19.09 nm, and 19.02 nm for NiO, chromium-doped, iron-doped, cobalt-doped, copper-doped, and zinc-doped NiO, respectively. The markedly elevated ε and δ values recorded in the chromium-doped nickel oxide sample substantiate the presence of enhanced crystal defects or structural disarray, which consequently results in diminished crystallite dimensions and reduced crystallinity. The FESEM examination revealed a homogeneous fine morphology, and the EDS spectra provided further substantiation of the existence of dopants within the NiO. All synthesized samples were found to be within the nanoscale, exhibiting a mean size range of 63 nm to 109 nm. This finding is consistent with the crystallite dimensions revealed through XRD analysis. The introduction of chromium, copper, zinc and cobalt ions into nickel oxide decreases grain size, signifying an increase in strain within the lattice and a limitation on its growth. On the other hand, the unmodified nickel oxide nanoparticles affirm the existence of fundamental constituents such as nickel and oxygen. Also, in doped samples, in addition to nickel and oxygen, the impurity elements such as zinc, cobalt, chromium, copper, and iron can be detected. Also, the specific surface area of the samples is 22.841, 37.331, 16.404, 42.197, 32.466, and 29.940 $m^2\Big/g$ calculated from the BET adsorption equation. Moreover, FTIR analyses confirmed the stretching and bending modes of the nanopowders. The distinct peaks associated with metal hydroxide (M-OH) framework bonds and metal-oxygen (M-O) interactions are prominently observed in the lower wavenumber region, specifically between 400 and 700 cm^{-1}. DRS investigations showed higher reflectance for Zn-doped and Fe-doped NiO samples and a decrease in bandgap for Co, Cr, Cu, or Fe-doped NiO, and a blue shift was detected in Zn-NiO compared to pristine NiO. The band gaps for pristine nickel oxide and

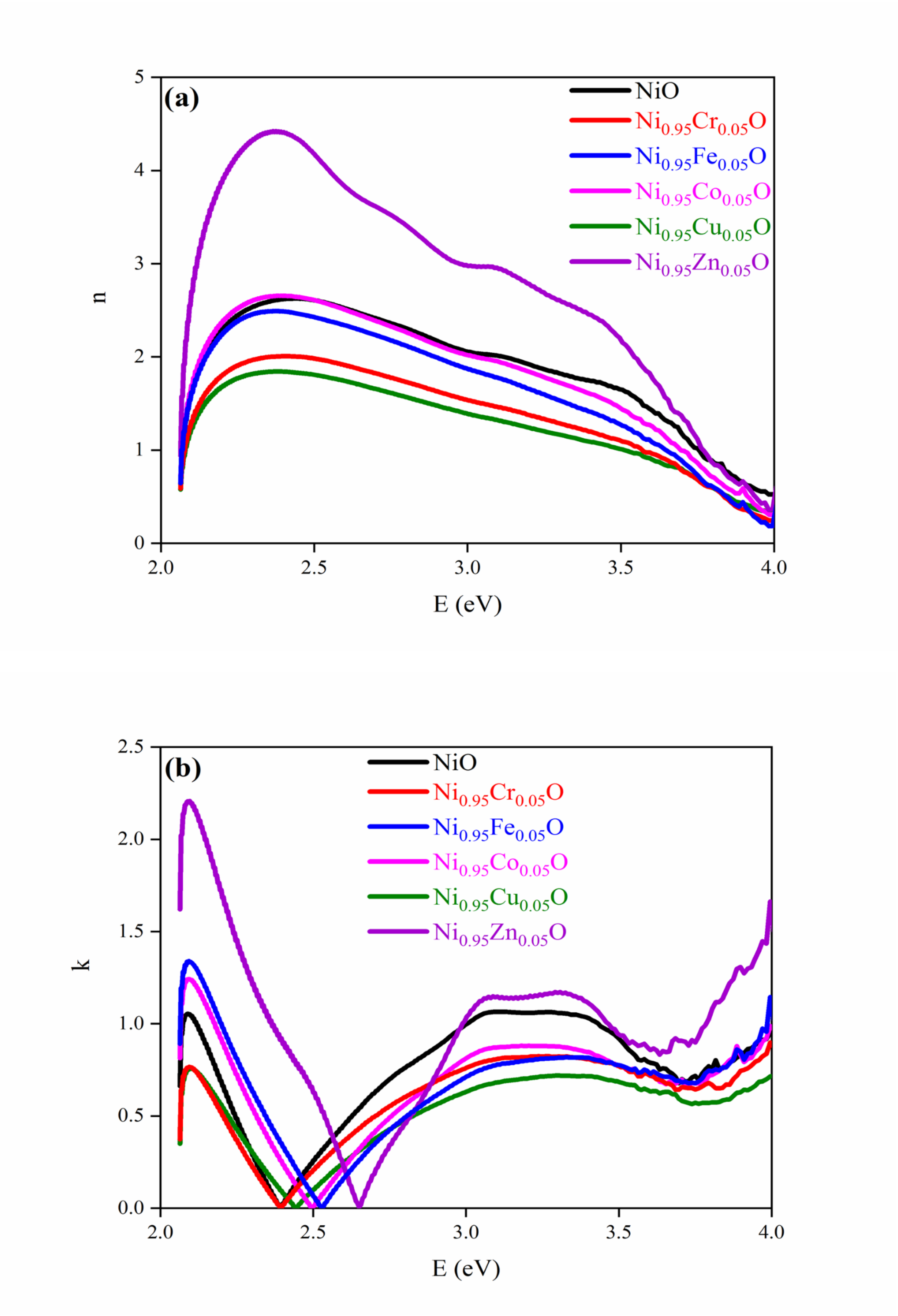

Fig. 9. **a** The real and **a** the imaginary portion of the complex refractive index versus hυ

nickel oxide doped with chromium, iron, cobalt, copper, and zinc are determined to be 3.41 eV, 3.07 eV, 3.17 eV, 3.33 eV, 2.77 eV, and 3.46 eV, respectively. These results indicate that the prepared pristine and doped NiO nanopowders have significant potential for utilization in optoelectronics and both linear and nonlinear optical device fields. Magnetic characteristics analyzed through VSM studies showed that the saturation magnetization exhibited values of 0.276 emu/g, 0.239 emu/g, 2.331 emu/g, 0.305 emu/g, 0.177 emu/g, and 0.260 emu/g for NiO, chromium-doped, iron-doped, cobalt-doped, copper-doped, and zinc-doped NiO, respectively. The magnetic properties of the nanopowders are intricately associated with their crystallinity, magnetic orientation, morphology, and particle dimensions. Furthermore, iron-doped nickel oxide nanoparticles exhibited a superior saturation magnetization value. They manifested pronounced ferromagnetic characteristics at ambient temperature due to iron substitution within the nickel oxide lattice. Therefore, the notable improvements in the magnetic and optical characteristics of the prepared nanopowders at atmosphere temperature, have proven to be potentially, confidently and highly beneficial for applications in data storage, magnetic, spintronic devices and optoelectronic devices.

Data availability

Data sets generated during the current study are available from the corresponding author on reasonable request.

Received: 31 July 2024; Accepted: 1 January 2025

References

1. Rahman, M. A., Radhakrishnan, R. & Gopalakrishnan, R. Structural, optical, magnetic and antibacterial properties of nd doped NiO nanoparticles prepared by co-precipitation method. *J. Alloys Compd.* **742**, 421–429 (2018).
2. Al Boukhari, J., Khalaf, A., Sayed Hassan, R. & Awad, R. Structural, optical and magnetic properties of pure and rare earth-doped NiO nanoparticles. *Appl. Phys. A*. **126**, 1–13 (2020).
3. Abdallah, A. M., Noun, M. & Awad, R. Dielectric, impedance and conductivity properties of pristine and (Gd, Ru)-dual doped NiO nanoparticles. *J. Alloys Compd.* **910**, 164952 (2022).
4. Al Boukhari, J., Azab, A. A., Bitar, Z. & Awad, R. Influence of (mg, Cu) codoping on the structural, optical and magnetic properties of NiO nanoparticles synthesized by coprecipitation method. *Phys. B Condens. Matter*. **663**, 415004 (2023).
5. Kisan, B., Bhuyan, R. K. & Mohapatra, R. K. Nanocrystalline NiO powder: synthesis, characterization and emerging applications. *Nano-Biosorbents Decontam Water Air Soil. Pollut.* **23**, 529–550 (2022).
6. Aytan, E. et al. Spin-phonon coupling in antiferromagnetic nickel oxide. *Appl. Phys. Lett.* **111**, 252402 (2017).
7. Panigrahi, U. K., Sathe, V., Babu, P. D., Mitra, A. & Mallick, P. Effect of mg doping on the improvement of photoluminescence and magnetic properties of NiO nanoparticles. *Nano Express*. **1**, 20009 (2020).
8. Peng, Z. et al. Managing the double-edged Sword of Ni3 + in sputter-deposited NiO x by Interfacial Redox Reactions for efficient Perovskite Solar cells. *ACS Appl. Energy Mater.* **6**, 1396–1403 (2023).
9. Powell, R. J. & Spicer, W. E. Optical properties of NiO and CoO. *Phys. Rev. B*. **2**, 2182 (1970).
10. Low, W. Paramagnetic and optical spectra of divalent nickel in cubic crystalline fields. *Phys. Rev.* **109**, 247 (1958).
11. Newman, R. & Chrenko, R. M. Optical properties of nickel oxide. *Phys. Rev.* **114**, 1507 (1959).
12. Tsuboi, T. & Kleemann, W. Fine structure of near infrared optical absorption in NiO. *J. Phys. Condens. Matter*. **6**, 8625 (1994).
13. Kuzmin, A., Purans, J. & Rodionov, A. X-ray absorption spectroscopy study of the Ni K edge in magnetron-sputtered nickel oxide thin films. *J. Phys. Condens. Matter*. **9**, 6979 (1997).
14. Miao, R., Zeng, W. & Gao, Q. SDS-assisted hydrothermal synthesis of NiO flake-flower architectures with enhanced gas-sensing properties. *Appl. Surf. Sci.* **384**, 304–310 (2016).
15. Karsthof, R., von Wenckstern, H., Olsen, V. S. & Grundmann, M. Identification of LiNi and VNi acceptor levels in doped nickel oxide. *APL Mater.* **8**, 121106 (2020).
16. Bayappagari, B., Shaik, K., Chakraborty, D. & Kunapalli, C. K. Structural, optical and magnetic properties of vacuum annealed Fe, Mn doped NiO nanoparticles. *Appl. Phys. A*. **127**, 1–9 (2021).
17. Rinaldi-Montes, N. et al. Interplay between microstructure and magnetism in NiO nanoparticles: breakdown of the antiferromagnetic order. *Nanoscale* **6**, 457–465 (2014).
18. Li, J. C., Hou, X. Y. & Cao, Q. Effect of Cu doping on the resistive switching of NiO thin films. *J. Appl. Phys.* **115**, 164507 (2014).
19. Yousaf, S. et al. Tuning the structural, optical and electrical properties of NiO nanoparticles prepared by wet chemical route. *Ceram. Int.* **46**, 3750–3758 (2020).
20. Menon, P. S. et al. Role of surface defects in the third order nonlinear optical properties of pristine NiO and cr doped NiO nanostructures. *Ceram. Int.* **49**, 5815–5827 (2023).
21. Huang, S. et al. Enhancing the performance of polymer solar cells using solution-processed copper doped nickel oxide nanoparticles as hole transport layer. *J. Colloid Interface Sci.* **535**, 308–317 (2019).
22. You, M., Kim, T. G. & Sung, Y. M. Synthesis of Cu-doped TiO2 nanorods with various aspect ratios and dopant concentrations. *Cryst. Growth Des.* **10**, 983–987 (2010).
23. Shannon, R. D. Revised effective ionic radii and systematic studies of interatomic distances in halides and chalcogenides. *Acta Crystallogr. Sect. A Cryst. physics, diffraction, Theor. Gen. Crystallogr.* 32, 751–767 (1976).
24. Allred, A. L. Electronegativity values from thermochemical data. *J. Inorg. Nucl. Chem.* **17**, 215–221 (1961).
25. Sharma, R. et al. Studies on the structure optical and electrical properties of Zn-doped NiO thin films grown by spray pyrolysis. *Optik (Stuttg).* **127**, 4661–4668 (2016).
26. Kisan, B., Kumar, J. & Alagarsamy, P. Room temperature ferromagnetism in Zn-doped NiO nanoparticles: an experimental and DFT + U approach. *J. Alloys Compd.* **868**, 159176 (2021).
27. Xue, J., Li, W., Song, Y., Li, Y. & Zhao, J. Visualization electrochromic-supercapacitor device based on porous Co doped NiO films. *J. Alloys Compd.* **857**, 158087 (2021).
28. Samidin, S. et al. Role of Cr-doped NiO in reduction under a low concentration of H2 and CO. *Surf. Interfaces*. **41**, 103106 (2023).
29. Ahmed, R. & Nabi, G. Enhanced electrochemical performance of Cr-doped NiO nanorods for supercapacitor application. *J. Energy Storage*. **33**, 102115 (2021).
30. Ponnusamy, P. M. et al. Structural, optical and magnetic properties of undoped NiO and Fe-doped NiO nanoparticles synthesized by wet-chemical process. *Mater. Charact.* **114**, 166–171 (2016).
31. Wang, J., Cai, J., Lin, Y. H. & Nan, C. W. Room-temperature ferromagnetism observed in Fe-doped NiO. *Appl. Phys. Lett.* **87**, 202501 (2005).
32. Manna, S. & De, S. K. Magnetic properties of Li and Fe co-doped NiO. *Solid State Commun.* **149**, 297–300 (2009).
33. Mishra, A. K., Bandyopadhyay, S. & Das, D. Structural and magnetic properties of pristine and Fe-doped NiO nanoparticles synthesized by the co-precipitation method. *Mater. Res. Bull.* **47**, 2288–2293 (2012).
34. Moraes, M. C. et al. NiO-promoted pt electrocatalysts prepared by thermal decomposition of polymeric precursors for oxidation of glycerol in alkaline medium. *J. Environ. Chem. Eng.* **7**, 102922 (2019).
35. Vivekanandan, A. K., Subash, V., Chen, S. & Chen, S. H. Sonochemical synthesis of nickel-manganous oxide nanocrumbs decorated partially reduced graphene oxide for efficient electrochemical reduction of metronidazole. *Ultrason. Sonochem*. **68**, 105176 (2020).
36. Poimenidis, I. A., Lykaki, M., Moustaizis, S., Loukakos, P. & Konsolakis, M. One-step solvothermal growth of NiO nanoparticles on nickel foam as a highly efficient electrocatalyst for hydrogen evolution reaction. *Mater. Chem. Phys.* **305**, 128007 (2023).

37. Zhu, L. et al. Hydrothermal preparation of NiO/La–NaTaO3 composite photocatalyst for degradation of ammonium dibutyl dithiophosphate wastewater. *Environ. Pollut*. **334**, 122139 (2023).
38. Tao, X. et al. Preparation of Co doped NiO thin films with excellent switching time and coloring efficiency through sol-gel spin coating. *Thin Solid Films* **779**, 139935 (2023).
39. Aziz, F. et al. Facile synthesis of NiO/ZnO nano-composite by co-precipitation, characterization and photocatalytic study of colored and colorless organic pollutants by solar irradiation. *Phys. B Condens. Matter*. **640**, 413858 (2022).
40. Quinten, M. *Optical Properties of Nanoparticle Systems: Mie and beyond* (Wiley, 2010).
41. Jafarzadeh, N. et al. Structural, optical and dielectric studies of Ag nanoparticles decorated by herceptin. *Phys. E Low-dimensional Syst. Nanostruct.* **114**, 113562 (2019).
42. Norouzzadeh, P., Mabhouti, K., Golzan, M. M. & Naderali, R. Consequence of Mn and Ni doping on structural, optical and magnetic characteristics of ZnO nanopowders: the Williamson–Hall method, the Kramers–Kronig approach and magnetic interactions. *Appl. Phys. A*. **126**, 154 (2020).
43. Krishnakanth, R., Jayakumar, G., Irudayaraj, A. A. & Raj, A. D. Structural and magnetic properties of NiO and Fe-doped NiO nanoparticles synthesized by chemical co-precipitation method. *Mater. Today Proc.* 3, 1370–1377 (2016).
44. Vallalperuman, K., Parthibavarman, M., Sathishkumar, S., Durairaj, M. & Thavamani, K. Synthesis and characterization of Co and Mn doped NiO nanoparticles. *Korean J. Chem. Eng.* **31**, 639–643 (2014).
45. Sheena, P. A., Hitha, H., Sreedevi, A. & Varghese, T. Microstructural characterization and modified spectral response of cobalt doped NiO nanoparticles. *Mater. Chem. Phys.* **229**, 412–420 (2019).
46. Mohapatra, M. & Anand, S. Synthesis and applications of nano-structured iron oxides/hydroxides–a review. *Int. J. Eng. Sci. Technol.* **2**, 127–146 (2010).
47. Varunkumar, K., Hussain, R., Hegde, G. & Ethiraj, A. S. Effect of calcination temperature on Cu doped NiO nanoparticles prepared via wet-chemical method: structural, optical and morphological studies. *Mater. Sci. Semicond. Process.* **66**, 149–156 (2017).
48. Larumbe, S. et al. Ni doped Fe3O4 magnetic nanoparticles. *J. Nanosci. Nanotechnol*. **12**, 2652–2660 (2012).
49. Jung, W. S., Oh, H., Kadam, A. N. & Lee, S. Calcination temperature effect on citrate-capped Iron Oxide nanoparticles as Lithium-Storage Anode materials. *Phys. Status Solidi*. **215**, 1701004 (2018).
50. Wahab, A. et al. Dye degradation property of cobalt and manganese doped iron oxide nanoparticles. *Appl. Nanosci.* **9**, 1823–1832 (2019).
51. Ogale, S. B., Venkatesan, T. V. & Blamire, M. *Functional Metal Oxides: New Science and Novel Applications* (Wiley, 2013).
52. Arif, M., Sanger, A., Shkir, M., Singh, A. & Katiyar, R. S. Influence of interparticle interaction on the structural, optical and magnetic properties of NiO nanoparticles. *Phys. B Condens. Matter*. **552**, 88–95 (2019).
53. Cai, M. J., Li, C. R. & He, L. Enhancing photothermal CO 2 catalysis by thermal insulating substrates. *Rare Met.* **39**, 881–886 (2020).
54. Li, P. et al. Cr-doped NiO nanoparticles as selective and stable gas sensor for ppb-level detection of benzyl mercaptan. *Sens. Actuators B Chem.* **339**, 129886 (2021).
55. Ahmed, A. A. A., Alahsab, E. A. A. & Abdulwahab, A. M. The influence of zn and mg doping on the structural and optical properties of NiO nano-structures for optoelectronic applications. *Results Phys.* **22**, 103938 (2021).
56. Mabhouti, K., Karamirad, M., Norouzzadeh, P., Golzan, M. M. & Naderali, R. Measurement of nickel doped zinc oxide NPs resonance frequencies and electromagnetic properties in X-Band. *Phys. B Condens. Matter*. **602**, 412532 (2021).
57. Norouzzadeh, P., Mabhouti, K., Golzan, M. M. & Naderali, R. Comparative study on dielectric and structural properties of undoped, Mn-doped, and Ni-doped ZnO nanoparticles by impedance spectroscopy analysis. *J. Mater. Sci. Mater. Electron.* **31**, 7335–7347 (2020).
58. Mabhouti, K., Norouzzadeh, P. & Taleb-Abbasi, M. Effects of Fe, Co, or Ni substitution for mn on La0. 7Sr0. 3MnO3 perovskite: structural, morphological, and optical analyses. *J. Non Cryst. Solids*. **610**, 122283 (2023).
59. Rini, A. S. Diffraction pattern simulation of crystal structure towards the ionic radius changes via vesta program. *J. Technomater. Phys.* **1**, 132–139 (2019).
60. Venkateswarlu, K., Sandhyarani, M., Nellaippan, T. A. & Rameshbabu, N. Estimation of crystallite size, lattice strain and dislocation density of nanocrystalline carbonate substituted hydroxyapatite by X-ray peak variance analysis. *Procedia Mater. Sci.* **5**, 212–221 (2014).
61. Shen, Y. et al. Effect of ionic size of dopants on the lattice structure, electrical and electrochemical properties of La2 − xMxNiO4 + δ (M = ba, Sr) cathode materials. *Int. J. Hydrogen Energy*. **39**, 1023–1029 (2014).
62. Vinod, G., Rajashekhar, K. & Naik, J. L. Dysprosium doped Cu0. 8Cd0. 2DyxFe2-xO4 nano ferrites: a combined impact of Dy3 + on enhanced physical, optical, magnetic, and DC-electrical properties. *Ceram. Int.* **49**, 2829–2851 (2023).
63. Vinod, G., Rajashekhar, K., Ravinder, D. & Naik, J. L. Structural, electrical, and magnetic properties of erbium (Er3+) substituted Cu–Cd nano-ferrites. *J. Mater. Sci. Mater. Electron.* **32**, 24069–24082 (2021).
64. Sagadevan, S. & Podder, J. Investigations on structural, optical, morphological and electrical properties of nickel oxide nanoparticles. *Int. J. Nanopart.* **8**, 289–301 (2015).
65. Ponnusamy, P. M., Agilan, S., Muthukumarasamy, N., Raja, M. & Velauthapillai, D. Studies on cobalt doped NiO nanoparticles prepared by simple chemical method. *J. Mater. Sci. Mater. Electron.* **27**, 399–406 (2016).
66. Khan, A., Saad, M., Kamal, T. & Rahman, F. Structural, morphological, optical and UV-light driven enhanced photocatalytic properties of Fe-doped NiO nanoparticles. *Mater. Chem. Phys.* **305**, 127923 (2023).
67. Khosrozadeh, M., Mabhouti, K., Norouzzadeh, P. & Naderali, R. Complex impedance spectroscopy, dielectric response, and magnetic properties of the La0. 7 Sr0. 3BO3 (B = mn, Fe, Co, or Ni) perovskite oxides. *Ceram. Int.* **50**, 315–328 (2024).
68. Itoh, Y., Katoh, K., Hirabayashi, K. & Murase, K. The relation between lattice-parameter and particle size in ZnS: Cu Phosphor. *Appl. Phys. A*. **26**, 227–230 (1981).
69. Prieur, D. et al. Size dependence of lattice parameter and electronic structure in CeO2 nanoparticles. *Inorg. Chem.* **59**, 5760–5767 (2020).
70. Brunauer, S., Emmett, P. H. & Teller, E. Adsorption of gases in multimolecular layers. *J. Am. Chem. Soc.* **60**, 309–319 (1938).
71. Serra, M., Salagre, P., Cesteros, Y., Medina, F. & Sueiras, J. E. Study of preparation conditions of NiO–MgO systems to control the morphology and particle size of the NiO phase. *Solid State Ion.*. **134**, 229–239 (2000).
72. Kalam, A., Al-Sehemi, A. G., Al-Shihri, A. S., Du, G. & Ahmad, T. Synthesis and characterization of NiO nanoparticles by thermal decomposition of nickel linoleate and their optical properties. *Mater. Char.* **68**, 77–81 (2012).
73. Dwivedi, S., Nayak, H. C., Parmar, S. S., Kumhar, R. P. & Rajput, S. Calcination temperature reflected structural, optical and magnetic properties of nickel oxide. *Magnetism* **2**, 45–55 (2022).
74. Gupta, P., Pandey, N. K., Kumar, K. & Yadav, B. C. Structural, optical and LPG sensing properties of zinc-doped nickel oxide pellets operated at room temperature. *Sens. Actuators Phys.* **319**, 112484 (2021).
75. Abdallah, A. M., Noun, M. & Awad, R. Tuning the structural, optical and magnetic properties of PVP-capped NiO nanoparticles by gadolinium doping. *Appl. Phys. A*. **127**, 1–15 (2021).
76. Kamalam, M. B. R., Inbanathan, S. S. R. & Sethuraman, K. Enhanced photo catalytic activity of graphene oxide/MoO3 nanocomposites in the degradation of Victoria Blue Dye under visible light irradiation. *Appl. Surf. Sci.* **449**, 685–696 (2018).
77. Gupta, P. et al. Influence of tin doping on the liquefied petroleum gas and humidity sensing properties of NiO nanoparticles. *J. Mater. Res.* **37**, 369–379 (2022).

78. Munawar, T., Iqbal, F., Yasmeen, S., Mahmood, K. & Hussain, A. Multi metal oxide NiO-CdO-ZnO nanocomposite–synthesis, structural, optical, electrical properties and enhanced sunlight driven photocatalytic activity. *Ceram. Int.* **46**, 2421–2437 (2020).
79. Aslinjensipriya, A., Reena, R. S., Infantiya, S. G., Ragu, R. & Das, S. J. Probing into the physicochemical consequences of pristine and X0. 06Ni0. 94O (X = Co, Fe, Cu) nanoparticles for bactericidal, antifungal and hemolytic competency. *J. Alloys Compd.* **938**, 168581 (2023).
80. Siddique, M. N. & Tripathi, P. Lattice defects formulated ferromagnetism in nonmagnetic La (III) ion doped NiO nanostructures: role of oxygen vacancy. *J. Alloys Compd.* **825**, 154071 (2020).
81. Vinod, G., Rajashekhar, K., Sandeep, Y. & Naik, J. L. Influence of RE-Gd3 + ion substitution on structure, morphology, optical, and magnetic analysis of Cu-Cd based nano ferrites synthesized by low-temperature citrate sol–gel auto combustion method. *J. Magn. Magn. Mater.* **562**, 169772 (2022).
82. Vinod, G. et al. Impact of cation distribution on structural, morphological, optical and low-temperature magnetic properties of Er3 + substituted Cu0. 8Cd0. 2Fe2O4 nanoparticles. *Inorg. Chem. Commun.* **159**, 111817 (2024).
83. Jharwal, S., Singh, P. K., Rana, D. K., Srivastava, M. K. & Kumar, A. Structural and magnetic properties of Cu and Mn co-doped NiO nanoparticles. *Mater. Today Proc.* 67, 648–651 (2022).
84. Bi, H., Li, S., Zhang, Y. & Du, Y. Ferromagnetic-like behavior of ultrafine NiO nanocrystallites. *J. Magn. Magn. Mater.* **277**, 363–367 (2004).
85. Chen, Z. Y. et al. Vacancy-induced ferromagnetic behavior in antiferromagnetic NiO nanoparticles: a positron annihilation study. *ECS J. Solid State Sci. Technol.* **6**, P798 (2017).
86. Layek, S. & Verma, H. C. Room temperature ferromagnetism in Mn-doped NiO nanoparticles. *J. Magn. Magn. Mater.* **397**, 73–78 (2016).
87. He, X. et al. Large exchange bias and enhanced coercivity in strongly-coupled Ni/NiO binary nanoparticles. *RSC Adv.* **9**, 30195–30206 (2019).
88. Cullity, B. D. & Graham, C. D. *Introduction to Magnetic Materials* (Wiley, 2011).
89. Hosny, N. M., Gomaa, I., El-Moemen, A., Anwar, Z. M. & A. & Synthesis, magnetic and adsorption of dye onto the surface of NiO nanoparticles. *J. Mater. Sci. Mater. Electron.* **31**, 8413–8422 (2020).
90. Suresh, R. et al. NiO nanoflakes: effect of anions on the structural, optical, morphological and magnetic properties. *J. Magn. Magn. Mater.* **441**, 787–794 (2017).
91. Panigrahi, U. K. et al. Zn doping induced enhancement of multifunctional properties in NiO nanoparticles. *J. Alloys Compd.* **833**, 155050 (2020).
92. Usharani, N. J. & Bhattacharya, S. S. Effect of defect states in the optical and magnetic properties of nanocrystalline NiO synthesised in a single step by an aerosol process. *Ceram. Int.* **46**, 5671–5680 (2020).
93. Moura, K. O. et al. Tuning the surface anisotropy in Fe-doped NiO nanoparticles. *Nanoscale* **6**, 352–357 (2014).
94. Kumar, S., Kim, Y. J., Koo, B. H. & Lee, C. G. Structural and magnetic properties of Ni doped CeO2 nanoparticles. *J. Nanosci. Nanotechnol.* **10**, 7204–7207 (2010).
95. Ijeh, R. O. et al. Magnetic and optical properties of electrodeposited nanospherical copper doped nickel oxide thin films. *Phys. E Low-dimensional Syst. Nanostruct.* **113**, 233–239 (2019).
96. Lin, Y. H. et al. Ferromagnetism and electrical transport in Fe-doped NiO. *Phys. Rev. B.* **73**, 193308 (2006).
97. Noipa, K., Labuayai, S., Swatsitang, E. & Maensiri, S. Room-temperature ferromagnetism in Nanocrystalline Fe-doped NiO powders synthesized by a simple direct thermal decomposition method. *Electron. Mater. Lett.* **10**, 147–152 (2014).
98. Manna, S., Deb, A. K., Jagannath, J. & De, S. K. Synthesis and room temperature ferromagnetism in Fe doped NiO nanorods. *J. Phys. Chem. C.* **112**, 10659–10662 (2008).
99. Pradeep, R. et al. Magnetic anomalies in Fe-doped NiO nanoparticle. *Mater. Res. Express.* **4**, 96103 (2017).
100. Bharathy, G. & Raji, P. Pseudocapacitance of Co doped NiO nanoparticles and its room temperature ferromagnetic behavior. *Phys. B Condens. Matter*. **530**, 75–81 (2018).
101. Ding, C. et al. Effects of Co2 + doping on physicochemical behaviors of hierarchical NiO nanostructure. *Appl. Surf. Sci.* **390**, 890–896 (2016).
102. Norouzzadeh, P., Golzan, M. M. & Naderali, R. Effect of Mn-substitution on impedance spectroscopy and magnetic properties of Al-doped ZnO nanoparticles. *Nanotechnology* **31**, 325704 (2020).
103. Mala, N. A., Dar, M. A., Sivakumar, S., Husain, S. & Batoo, K. M. Enhanced electrochemical properties of zinc and manganese co-doped NiO nanostructures for its high-performance supercapacitor applications. *Inorg. Chem. Commun.* **142**, 109661 (2022).
104. Skomski, R. *Simple Models of Magnetism* (Oxford University Press, 2008).
105. Bhowmik, R. N., Kazhugasalamoorthy, S. & Sinha, A. K. Role of initial heat treatment of the ferrite component on magnetic properties in the composite of ferrimagnetic Co1. 75Fe1. 25O4 ferrite and non-magnetic BaTiO3 oxide. *J. Magn. Magn. Mater.* **444**, 451–466 (2017).
106. Ashokkumar, T., Rajadurai, A. & Gopinath, S. C. B. A study of magnetic retardation of iron-nickel nanopowder and sintered specimen by spark plasma. *J. Magn. Magn. Mater.* **485**, 280–285 (2019).
107. Sahoo, V., Bhowmik, R. N. & Khan, S. A. Enhancement of electrical conductivity, optical band gap and ferromagnetic properties by co-doping of Co and Ti ions in canted antiferromagnetic hematite (α-Fe2O3) system. *Mater. Chem. Phys.* **296**, 127298 (2023).
108. Sharma, K. R. & Negi, N. S. Doping effect of cobalt on various properties of nickel oxide prepared by solution combustion method. *J. Supercond Nov Magn.* **34**, 633–645 (2021).
109. Rashid, A. & Ikram, M. Optical characterization of La2SrFe2TiO9 triple perovskite: insights for advanced optoelectronic and solar cell applications. *Optik (Stuttg)*. **308**, 171843 (2024).
110. Absi, E. et al. Characterisation of binary (NiO) x (Ag2O) 1 – x nanoparticles synthesised via the thermal treatment route. *Ceram. Int.* **49**, 19194–19205 (2023).
111. Norouzzadeh, P., Mabhouti, K., Golzan, M. M. & Naderali, R. Investigation of structural, morphological and optical characteristics of mn substituted Al-doped ZnO NPs: a Urbach energy and kramers-Kronig study. *Optik* **204***,* 164227 (2020).
112. Agrawal, S., Parveen, A. & Azam, A. Microwave assisted synthesis of Co doped NiO nanoparticles and its fluorescence properties. *J. Lumin.* **184**, 250–255 (2017).
113. Al-Saeedi, S. I., Al-Senani, G. M., Abd-Elkader, O. H. & Deraz, N. M. One pot synthesis, surface and magnetic properties of Cu2O/Cu and Cu2O/CuO nanocomposites. *Crystals* **11**, 751 (2021).
114. Patel, K. N. et al. Structural and optical analysis of Fe doped NiO nanoparticles synthesized by chemical precipitation route. *Mater. Res. Bull.* **106**, 187–196 (2018).
115. Mabhouti, K. & Norouzzadeh, P. Notes on linear and non-linear optical characteristics of the nickel and manganese doped zinc oxide nanoparticles. *Optik (Stuttg)*. **231**, 166465 (2021).

Author contributions

FA: Investigation, Writing original draft. KM: Conceptualization, Data curation, Software, Editing original draft. AJ: Supervision. MT-A: Formal analysis, Writing original draft, Data curation.

Funding

This research did not receive any specific grant from funding agencies in the public, commercial, or not-for-profit sectors.

Declarations

Competing interests

The authors declare no competing interests.

Additional information

Supplementary Information The online version contains supplementary material available at https://doi.org/10.1038/s41598-025-85239-0.

Correspondence and requests for materials should be addressed to K.M.

Reprints and permissions information is available at www.nature.com/reprints.

Publisher's note Springer Nature remains neutral with regard to jurisdictional claims in published maps and institutional affiliations.

Open Access This article is licensed under a Creative Commons Attribution-NonCommercial-NoDerivatives 4.0 International License, which permits any non-commercial use, sharing, distribution and reproduction in any medium or format, as long as you give appropriate credit to the original author(s) and the source, provide a link to the Creative Commons licence, and indicate if you modified the licensed material. You do not have permission under this licence to share adapted material derived from this article or parts of it. The images or other third party material in this article are included in the article's Creative Commons licence, unless indicated otherwise in a credit line to the material. If material is not included in the article's Creative Commons licence and your intended use is not permitted by statutory regulation or exceeds the permitted use, you will need to obtain permission directly from the copyright holder. To view a copy of this licence, visit http://creativecommons.org/licenses/by-nc-nd/4.0/.

© The Author(s) 2025